國立交通大學

光電工程研究所

碩士論文

可同時量測光學晶體厚度及光軸之影像式偏極光測量方法

An Imaging Polarimetric Technique for Measuring both the Thickness and Optic-axis of a Uniaxial Film

研究生：李建立

指導教授：黃中垚

中華民國九十三年六月

可同時量測光學晶體厚度及光軸之影像式偏極光測量方法

An Imaging Polarimetric Technique for Measuring both the Thickness and Optic-axis of a Uniaxial Film

研究生：李建立　　Student: Chien-Li Lee

指導教授：黃中垚　　Advisor: Jung Y. Huang

國立交通大學

光電工程研究所

碩士論文

A Thesis

Submitted to Institute of Electro-Optical Engineering
College of Electronic Engineering and Computer Science
National Chiao Tung University
In Partial Fulfillment of the Requirement
For the Degree of
Master
In
Electro-Optical Engineering
June 2004
Hsinchu, Taiwan, Republic of China

中華民國九十三年六月

可同時量測光學晶體厚度及光軸之影像式偏極光測量方法

研究生：李建立　　指導教授：黃中垚

國立交通大學研究所

摘　要

我們提出一個影像式偏極光量測系統，可同時量厚度與光軸方向的二維分佈。此設計結合了影像式偏光儀和旋轉樣品的方法並且可以量測從 1μm 到 mm 等級的膜厚。其平面的解析度可達 100 μm。我們成功的驗證其功能於一個厚度為 1-mm 的 $LiNbO_3$、厚度為 4.9-μm 的液晶樣品和厚度為 10-μm 的空間光調制器(SLM)。最後，液晶光軸的指向在 Néel wall 附近和 Néel wall 結合點缺陷下的排列也被觀測並討論。Néel wall 在電場作用下的行為也被觀測並討論。

An Imaging Polarimetric Technique for Measuring both the Thickness and Optic-axis of a Uniaxial Film

Student: Chien-Li Lee Advisor: Professor Jung Y. Huang

Institute of Electro-Optical Engineering

National Chiao Tung University

Abstract

An imaging polarimetry and data acquisition procedures are designed for determining two-dimensional distributions of the thickness and optical axis of an optical uniaxial film. Our design combines an imaging polarimeter with rotation sample scheme and can be employed for monitoring film thickness from 1 μm to mm with an in-plane spatial resolution better than 100 μm. We successfully demonstrate the functionality with a 1-mm thick stoichiometric $LiNbO_3$ wafer, 4.9-μm thick liquid crystal device and 10-μm thick spatial light modulator (SLM).The LC director's orientation of Néel wall with and without a point defect have been observed and discussed.The behavior of a Néel wall under applied electric field have been observed and discussed.

誌　謝

感謝神，我親愛的主耶穌，這一路的引領和眷顧，不僅在環境中祝福了我的學業，更寶貝祂以祂這包羅萬有、賜生命的那靈在內裏的運行，為著將祂那追測不盡的豐富分賜到我裏面，使我們成為祂的豐滿，成就祂永遠的計劃、經綸。如今，這兩年所學得一些推羅的技巧必須死去，好在復活裏為神建造所用。

感謝在弟兄姊妹之家的每一位，陪伴著我一同成長。是主使我們調在一起且能彼此相愛，為著建造祂生機的身體！有首詩歌說：「晨光中我們進入主的話，星月下每張臉笑如花，這等生活神聖美如畫…」，相信我們走過日子在永世的新耶路撒冷還要再紀念。

感謝老師悉心指導，傳授與我屬世學問和研究態度。願老師經歷主作那真實的滿足、喜樂和永遠的盼望。實驗室的文慈學姊、明彰、亦彥、立志，願你們在漫長的人生中找到人生的意義。願主祝福你們。

CONTENTS

LIST OF FIGURES

Chapter1

Introduction

1-1 Motivation

The application of uniaxial crystalline film had gained its wide spread popularity in recent years. There has been a great demand for a proper polarimetric technique to provide both the thickness and optic-axis orientation of a uniaxial film. The apparatus shall also be useful for applications ranging from quality assurance of crystal wafer for optical waveguides and solid-state laser applications [1], process control of liquid crystal device fabrication [2], to biomedical sensing [3]. Among these applications, imaging ability with an array detector to yield two-dimensional distributions of film thickness and optic-axis orientation is highly desirable.

For an example, the exhibiting function of LCD is via anisotropic properties of LCD

film used. In this regard, the measurement of the thickness and orientation of the optic-axis of a LC film is very important. Polarimetry is an important technique for investigating optical properties of uniaxial film. However, at this moment there is no imaging polarimetric system that can be used to yield the optical crystal thickness and the optic axis direction simultaneously.

1-2 Literature Survey and Technology Assessment

There are several useful material parameters that can be deduced by polarimetry. These parameters include film thickness, retardation, tilted angle, *etc*. In the following, we shall survey various polarimetric techniques and briefly comment on their principles and limitation of application.

In the reference [1], Nishida and Yamanaka reported a two-dimensional birefringence distribution measurement system for probing the thermal stress distribution induced by pump laser. The authors of this paper assume the laser rod to be uniaxial with an in-plane optic axis. The thermally induced anisotropy is therefore assumed to along the radial direction; therefore the effective optical axis is perpendicular to the pump direction. The technique does not consider the case of tilting optic-axis from sample surface and no information about sample thickness is provided.

The second type of polarimetric system [2] deduces the pretilt of optic axis by

rotating the specimen. When the specimen is rotated to a specific angle, where the optical beam used propagates along the optic axis or its vertical direction. In this case, the pretilt of optic-axis can be determined from the extreme angle of the curve of optical transmittance-vs.-incident angle. This method can only be applied on samples with pretilt angle lying between 0°~20° or 70°~90°. In addition, the film thickness cannot be obtained simultaneously.

The third method [4] extends the measuring range of pretilt angle to 20°-70°. By changing the rotation angle of a sample, a periodic variation of the optical transmission is found, and the optic axis pretilt angle is inferred with two incident angles of adjacent maximum (brightest) and minimum (darkest) transmission. This method however is not suitable for specimens thicker than 20μm, where no two adjacent maximum and minimum transmission intensities can be found. Although this method can improve the limitation of the measuring range for the pretilt angle of optic axis, no information about film thickness is yielded. This method is only applicable for single point measurement with a laser beam and cannot be extended to deduce two-dimensional distribution of optic-axis.

The fourth method [5] strongly focuses light onto a specimen with an objective lens.

The pretilt angle of the sample can be obtained by measuring the lateral shift of the interference pattern of the transmission light on a screen. The drawback of this method is that a lens with large numerical aperture is required, and only the pretilt angle of the sample at the focus point can be measured. The measurable range of pretilt angle is limited to be 0°-20° or 70°-90°, and the thickness parameter is lost.

The fifth method [6] employs an ellipsometery. By changing the angles of polarizer and analyzer of the ellipsometer, the transmissive intensity of a spectrum can be zero at a specific wavelength (null transmission), and the twist angle of optic axis and the retardation of a uniaxial film can be obtained. However, when the specimen is thick (<3μm), the measured spectrum curve becomes wide. Therefore the wavelength which corresponds to the null transmission cannot be determined accurately. Furthermore, the measured retardation is coupled with film thickness and pretilt angle, so one of the two parameters shall be known in advance in order to determine the other. In addition, this method utilizes a spectrometer and is therefore only suitable for single point measurement.

The sixth method [7] also uses an ellipsometery. By measuring a total intensity ratio between any two spectrums, the thickness of the specimen can be obtained. This method

assumes the pretilt of the optic axis is small and therefore the retardation effect from the small pretilt angle can be neglected. So when the pretilt is large, another method is needed to measure the pretilt angle of the optic axis in advance. In addition, this method also utilizes spectrometer and is only suitable for single point measurement.

The above-mentioned polarimeters can only measure the thickness or the optic axis, and cannot measure both of them at the same time. Most systems are only suitable for single point measurement. If more material parameters are needed, different measurement systems are required. Hence, an apparatus which can yield the two-dimensional distributions of thickness and optic axis pretilt is highly demanded.

A polarimetric instrument measures the change in the polarization state of an optical beam after the beam passes through a sample and can be employed to ascertain the properties of a material. A typical setup of a polarimeter places a sample under test between a polarization state generator (PSG) and a polarization-state analyzer (PSA) [8]. Depending upon the application purpose, there are generally two categories of polarimeters to fit into the need: the 1st category belongs to a combination of single channel detector (*i.e.*, a photo diode) and photo-elastic modulator (PEM) for high precision applications (～0.01%). This type of polarimeter is suited to single point detection with high precision. The 2nd category is an imaging polarimetry with an array

detector. The method often yields a moderate precision of about 1%. Our apparatus belongs to this category.

The parameter measured with a polarimetry is phase retardance, which a product of film thickness and tilted angle of optic axis. Therefore, how to simultaneously deduce the optical crystal thickness and the optic axis direction is the main objective of this research.

1-3 Outline of the Thesis

In Chapter 2, we shall describe the principle of the measurement principle and the related data acquisition procedure. The feasibility study of the technique is then presented by measuring a variety of samples with different thicknesses, which include a single crystal $LiNbO_3$ wafer, a home-made liquid crystal, and a commercial LC spatial light modulator.

In Chapter 3, we present a study of LC alignment on a photopolymer substrate with a weak anchoring strength by using our imaging polarimetric technique. Due to the weak azimuthal anchoring the LC sample exhibits a common defect of Néel wall. We discuss the generation mechanism of a Néel wall and its director arrangement around the defect. We found the width of the Néel wall to shrink with an applied electric field.

Chapter 2
The Principle of the Measurement

2-1 Experimental Implementation

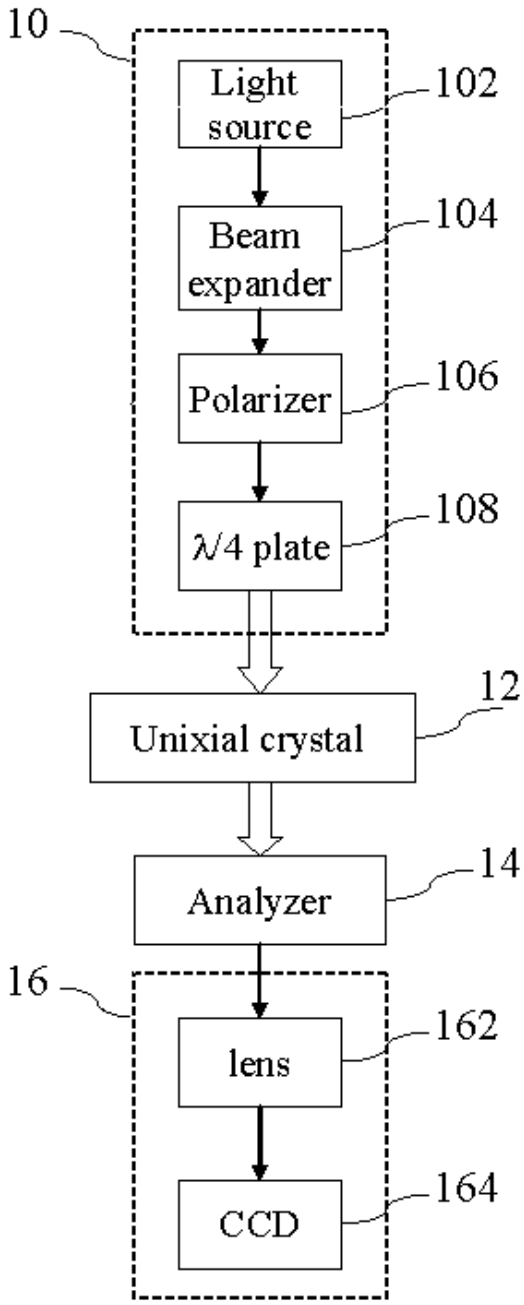

Fig.2-1 Schematic diagram of the system

Fig.2-1 shows the schematic diagram of our imaging polarimetric system, which is divided into the following four parts: a polarizing apparatus 10, a specimen stage, an analyzer 14 and an image detecting apparatus 16. A sample 12, which is a uniaxial crystal film, is located on the specimen stage. The polarizing apparatus 10 includes a light source 102, which is a He-Ne laser with wavelength 632 nm. The light beam expands to a light with uniform intensity via a 40-times beam expander 104, and becomes a right-circularly polarized light via a polarizer 106 and a quarter-wave plate 108. The analyzer 14 is generally a polarizer that transmits the polarized light passing through the specimen 12 to the variation diagram of the light intensity for analyzing the polarization state of the polarized light passing through the specimen 12. The image detecting apparatus 16 includes a lens 162 and a charge coupled device (CCD) 164. After the polarizing apparatus 10 produces a right-circularly light, the righ-thand-circularly light is injected into the specimen 12. The transmitting light passes through the analyzer 14, which is oriented to an azimuthal angle of ϕ, and is imaged onto the CCD 164 via the lens 162 according to requirement.

A 2D charge coupled device (CCD) is used as the array detector. It has an imaging area of 7×5 mm^2 and pixel elements of 426(H) ×320(V). The 2D intensity distribution measured by the CCD camera is transformed to National Television System Committee (NTSC) signal and sent to a computer which contains an image processing circuit board. The image processing board has picture elements of 640(H) ×480(V), each with 8-bit coding. To reduce the memory storage, we render nine (3×3) elements into one to yield a smaller size of 34,000 elements. We used Matlab as our imaging processing platform.

2-2 Principle of Measurement

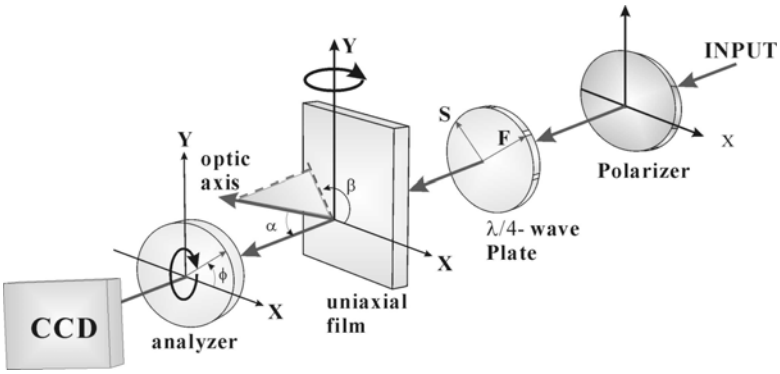

Fig.2-2 Schematic of our experimental setup

Fig. 2-2 depicts a schematic diagram showing the setup used for interpreting our polarimetric apparatus. The sample plane is defined as x-y plane, and the polar angle of the optic axis of the sample is defined to be α between the optic axis and the z-axis. The optic axis is projected onto the x-y plane to have an azimuthal angle of β relative to the x-axis.

By using Jones calculus, we can derive an expression for the optical irradiance on each pixel of CCD camera [1]:

$$\begin{bmatrix} E_x' \\ E_y' \end{bmatrix} = J_{PSA} J_f J_{PSG} E_{in} = E_0 \begin{bmatrix} \cos^2\phi & \sin\phi\cos\phi \\ \sin\phi\cos\phi & \sin^2\phi \end{bmatrix} \begin{bmatrix} \xi & \eta \\ \eta & \varsigma \end{bmatrix} \frac{1}{\sqrt{2}} \begin{bmatrix} 1 & i \\ i & 1 \end{bmatrix} \begin{bmatrix} 1 \\ 0 \end{bmatrix}. \quad (2.1)$$

Assuming the uniaxial sample to be oriented to have its optic axis pointed with polar angle α relative the beam propagation direction (the z-axis) and azimuthal angle β relative to the x-axis, the Jones matrix elements (J_f) of a uniaxial film are [9]

$$\begin{aligned}\xi &= \cos^2\beta\, e^{i\delta/2} + \sin^2\beta\, e^{-i\delta/2},\\ \eta &= i\sin 2\beta\, \sin(\delta/2),\\ \varsigma &= \cos^2\beta\, e^{-i\delta/2} + \sin^2\beta\, e^{i\delta/2}.\end{aligned} \qquad (2.2)$$

For a normal incidence with ψ=0, the retardance of the transmitted light becomes

$$\delta(\alpha) = \left(\frac{2\pi}{\lambda}\right) h \left(\frac{1}{\sqrt{\frac{1}{n_e^2}\sin^2\alpha + \frac{1}{n_o^2}\cos^2\alpha}} - n_o \right), \qquad (2.3)$$

where *h* denotes the film thickness. Here we assume that the index of refraction of the film to be uniform over the film thickness, and the indices are known *a priori*. By using Eq.(2.1), the optical intensity on the detector can be expressed as

$$I = E_x' E_x'^* + E_y' E_y'^* = \frac{I_0}{2}\{1 + \sin 2(\phi - \beta)\sin\delta\}, \qquad (2.4)$$

where I_0 denotes the incident beam intensity, and ϕ is the azimuthal angle of the PSA.

2-2-1 Principle to measure azimuthal angle (β)

First, we want to emphasize that $\sin\delta$ is a constant because retardation is a function of polar angle and specimen thickness which are kept constant during the measurement (see Eq.(2.1)).

We can determine the azimuthal angle β of the optic axis by fitting the measured intensity pattern $I(\phi)$ at normal incidence to Eq.(2.4) with $\sin\delta$ and β as the fitting parameters. For example, the angle ϕ is rotated from 0° to 180° and takes pictures with the CCD every 10 degrees of ϕ, nineteen pictures can be obtained. This yields a 19-points intensity curve for each pixel, which is then fitted to Eq.(2.4) to deduce β of each pixel.

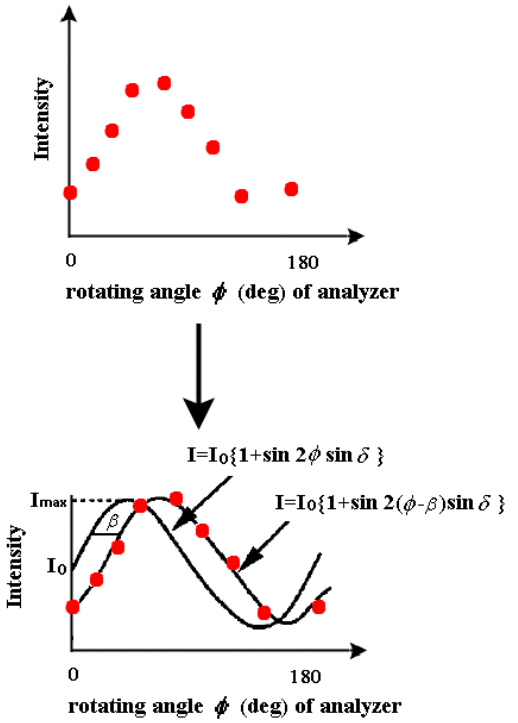

Fig.2-3 Determination of β and δ from optical intensity measured on a birefringent material

In more detail, the curve of sin 2(ϕ–β) shown in Fig.2-3 is fitted by the nonlinear least-squares method to each of the 19-points curves from the images. Second, the relative phase difference δ is determined from the position of the maximum amplitude by:

$$\sin 2(\varphi_m - \beta) = 1. \qquad (2.5)$$

This yields $\delta = \sin^{-1}\{I/(I_0/2) - 1\}$. Here β is an angular shift and is determined by $\beta = \phi_m - \pi/4$, ϕ_m denotes the rotational angle with the maximum amplitude.

From equation (2.4), when the value of sin(δ) is negative, the maximum amplitude is obtained with $\sin 2(\varphi_m - \beta) = -1$. The resulting β should add $\pi/2$ to yield a correct value. We can remove the quarter-wave plate and let the incident light to be x-polarized. This arrangement corresponds to a simple polarimetric geometry, which had been known

as conoscope as shown in Fig.2-4.

We then rotate the sample such that the projected optic-axis to be along the x axis (*i.e.*, β=0) and then change the incident angle by rotating the sample about y-axis. If the measured β angle is correct, there shall be no intensity variation when rotating the specimen about y-axis, as illustrated in Fig.2-5. This is because the principle plane (pp) is x-y plane and it does not change by the rotation about y-axis. The x-polarized incident light always observes an index of refraction of n_e. But when we rotate the sample to make $\beta = \pi/2$ and then rotate the sample about y-axis. We can always detect the intensity variation. This is because in this case the principle plane changes when the sample is rotated about y-axis. The x-polarized incident light will experience both n_e and n_o and change the polarization state. The leads to a variation of intensity (Fig.2-5).

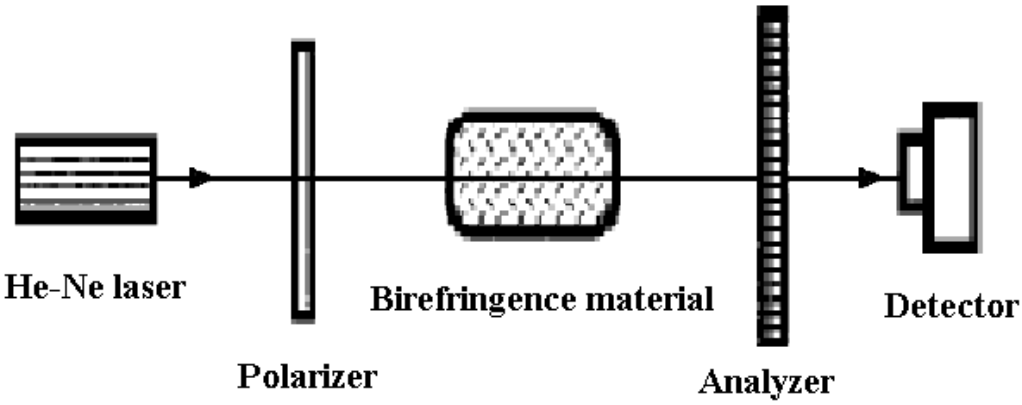

Fig.2-4 Schematic arrangement of a conventional conoscope

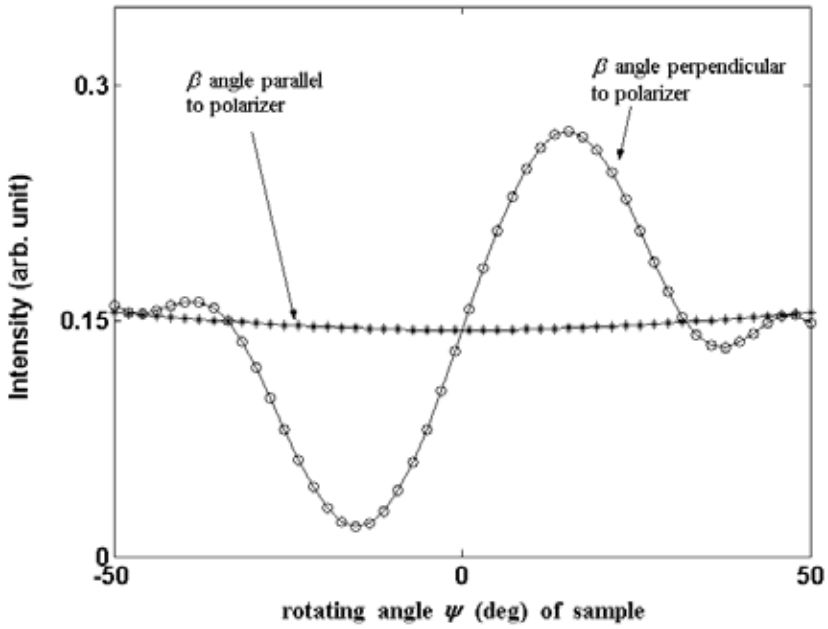

Fig.2-5 Intensity variation with in-plane optic-axis parallel to polarizer or perpendicular to polarizer when the quarter-wave plate is removed.

The intensity by using an arrangement of conventional conoscope can be expressed as:

$$I = I_0\left\{1-\sin^2(2\phi)\sin^2(\delta/2)\right\}, \qquad (2.6)$$

where I_0 is the incident intensity, ϕ is the angle between the polarizer and one of the principal axis of the uniaxial film, and δ denotes the relative phase shift. By comparing Eq.(2.6) to Eq.(2.4), we find that the conoscope exhibits two disadvantages: First, for $\delta<\pi/4$, $\sin^2(\delta/2)$ in Eq.(2.6) is smaller than $\sin\delta$ of Eq.(2.4). Thus, the conoscope has a lower sensitivity than the polarimeter used here. Fig.2-6 presents a sensitivity comparison of the polarimeter ($\sin\delta$) and conoscope ($\sin^2(\delta/2)$). Second, although the absolute value of δ can be obtained with conoscope, the technique can not distinguish the sign of δ. Therefore, the polarimeter used here is superior to the conventional conoscope and is more suited for measuring weakly birefringent samples.

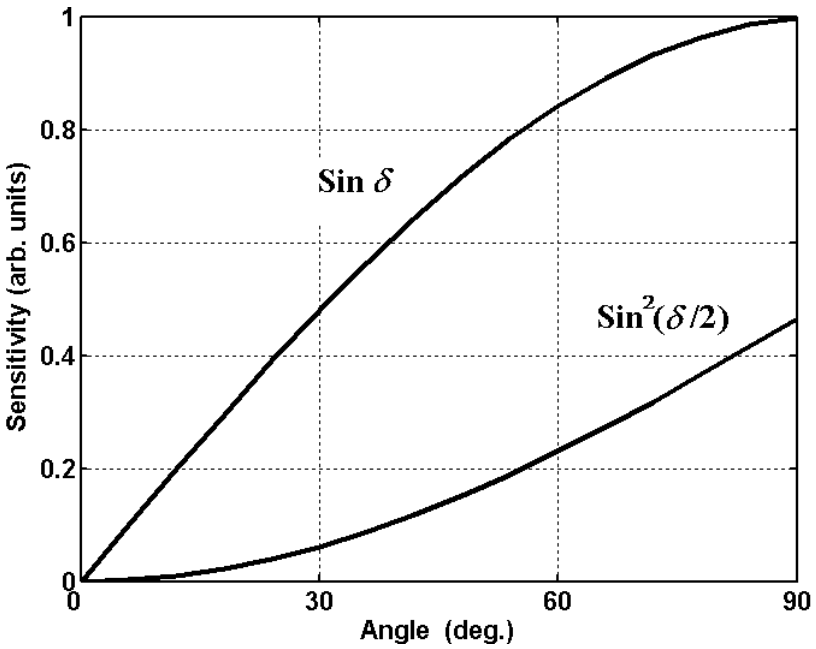

Fig . 2-6 Sensitivity comparison of polarimeter (sinδ) and conoscope (sin^2(δ/2)).

2-2-2 Principle to Measure Polar Angle (α) and Film Thickness

After the value of the angle β is determined, polar angle α of optic axis and thickness of the specimen can be deduced by first rotating sample along the z-axis such that $\sin 2(\phi-\beta)=1$ (i.e., $\phi-\beta=\pi/4$) for fixed ϕ. We then change the incident angle by rotating the specimen about the y-axis. The incident angle between the incident light and a sample normal is denoted by ψ, as shown in Fig.2-7.

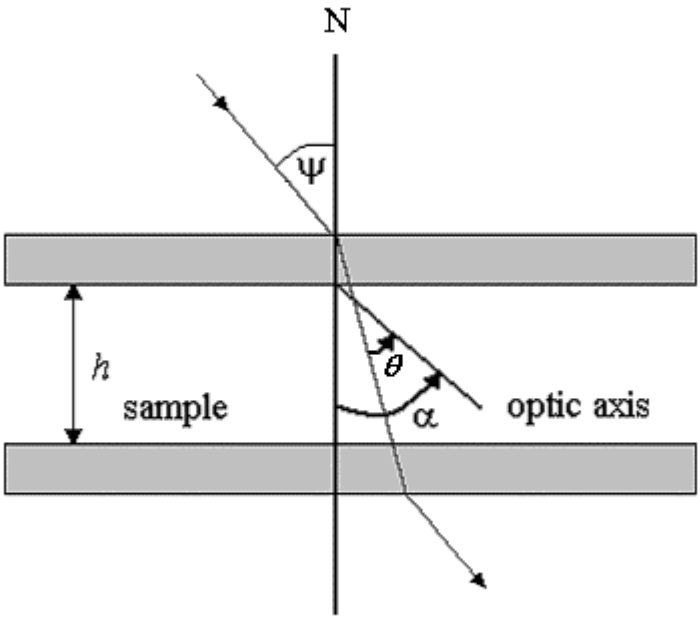

Fig.2-7 The geometry of an incident optical beam on a uniaxial crystal film

When the obliquely incident light passes through the specimen, the optical retardation experienced can be expressed as

$$\delta(\gamma,\psi)=\left(\frac{2\pi}{\lambda}\right)\cdot h\cdot f(\gamma,\psi) \tag{2.7}$$

where $\gamma \equiv \pi/2-\alpha$, and $f(\gamma,\psi)$ is shown as [2]：

$$f(\gamma,\psi)=\frac{1}{c^2}\left(a^2-b^2\right)\sin\gamma\cos\gamma\sin\psi+\frac{1}{c}\left(1-\frac{a^2b^2}{c^2}\cdot\sin^2\psi\right)^{1/2}-\frac{1}{b}\left(1-b^2\sin^2\psi\right)^{1/2} \tag{2.8}$$

$$a=\frac{1}{n_1},\quad b=\frac{1}{n_2},\quad c^2=a^2\cos^2\gamma+b^2\sin^2\gamma,$$

where n_1 and n_2 denote the refractive indexes of the extraordinary and the ordinary waves in a uniaxial film. We first note that when the polar angle α is fixed, γ is fixed too. We can be rewrite the optical transmittance as

$$T(\psi)=\frac{1}{2}\cdot\left(1+\sin\delta(\psi)\right) \tag{2.9}$$

Eq.(2.9) depicts that the optical transmittance varies with the incident angle of the

uniaxial film. The variation pattern also depends on the polar angle α of the optic axis and the thickness h of the uniaxial film. Therefore after obtaining a measured curve, we can fit the curve to Eq.(2.9) to deduce α and h. The intensity variation patterns for each pixel can be recovered and curve-fitted to Eq.(2.9) to form the 2-dimentional distribution of the film thickness and the axis polar angle.

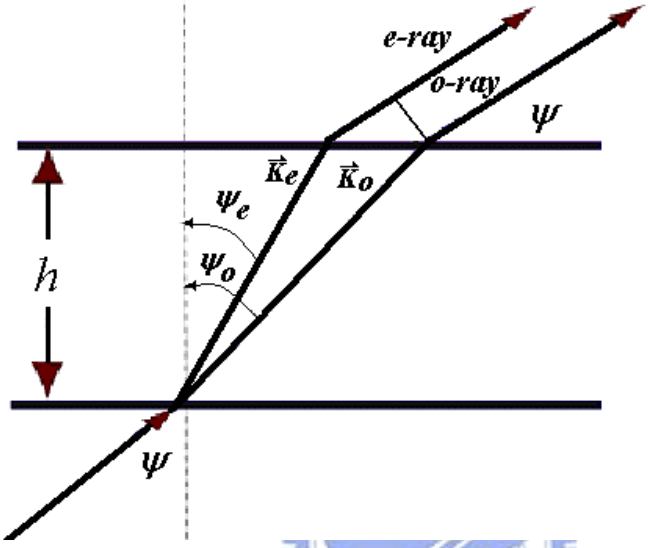

Fig .2-8 The geometry of an incident optical beam on a uniaxial crystal film which is divided into ordinary and extraordinary rays

For a horizontally aligned LC cell as an example, the pre-tilted angle of the optic axis is γ and incident angle is ψ. We can express the LC director and optical wave vector to be:

$$\vec{n} = (\cos\gamma, 0, \sin\gamma)$$

$$\vec{K} = (\sin\psi, 0, \cos\psi)$$

$$\vec{K}_e = (\sin\psi_e, 0, \cos\psi_e)$$

$$\vec{K}_o = (\sin\psi_o, 0, \cos\psi_o)\ .$$

By using the Snell's law:

$$\sin\psi = n_o \sin\psi_o = n_e \sin\psi_e$$

the effective refractive index of extraordinary can be expressed:

$$n_{eff}(\theta) = \frac{n_e}{\sqrt{[(n_e / n_o)^2 - 1]\cos^2\theta + 1}}$$

where θ denotes the angle between $\vec{K}_e$ and $\vec{n}$ with

$$\cos\theta = \vec{n} \bullet \vec{K} = \cos\alpha \sin\varphi_e + \sin\alpha \cos\varphi_e .$$

The optical path of o-ray and e-ray through the LC film can be expressed as:

$$\ell_e = \int_0^h \frac{n_{eff}(\theta)}{\cos\varphi_e} + (\tan\varphi_o - \tan\varphi_o)\sin\varphi] \; dz$$

$$\ell_o = \frac{n_o h}{\cos\psi_o} \quad ,$$

this yields

$$\ell_e - \ell_o = \int_0^h [(\frac{n_{eff}(\theta)}{\cos\psi_e} - \tan\psi_e \sin\psi) - (\frac{n_o}{\cos\varphi_o} - \tan\psi_o \sin\psi)]dz$$

$$= \int_0^h \{[\frac{n_{eff}(\theta)}{\cos\psi_e}(1-\sin\psi_e^2)] - [\frac{n_o}{\cos\psi_o}(1-\sin\psi_o^2)]\}dz$$

$$\ell_e - \ell_o = \int_0^h (n_{eff}(\theta)\cos\psi_e - n_o \cos\psi_o)dz .$$

Assume pre-tilted angle along z-direction to be uniform, then:

$$\delta(\psi) = \frac{2\pi h}{\lambda}[\frac{(n_o^2 - n_e^2)\sin\gamma\cos\gamma\sin\psi}{n_o^2\cos^2\gamma + n_e^2\sin^2\gamma} + \frac{n_e n_o}{\sqrt{n_o^2\cos^2\gamma + n_e^2\sin^2\gamma}}\sqrt{1 - \frac{\sin^2\psi}{n_o^2\cos^2\gamma + n_e^2\sin^2\gamma}} - \sqrt{n_o^2 - \sin^2\psi}] \quad . \qquad (2.10)$$

Method to obtain tilted angle from extremum angles (max/min values) of optical transmittance

A typical method [5] to measure the tilted angle of optic axis of a uniaxial film is to locate the extremum angles of optical transmittance. From Eq.(2.10), we can locate these extremum angles by taking a derivative of Ψ:

$\left.\frac{\partial\delta(\psi)}{\partial\psi}\right|_{\psi=\psi_x} = 0$, which yields

$$(n_o^2 - n_e^2)\sin\gamma\cos\gamma - \frac{n_o}{n_e}\frac{n_e^2\sin\psi_x}{\sqrt{n_o^2\cos^2\gamma + n_e^2\sin^2\gamma - \sin^2\psi_x}} + \frac{(n_o^2\cos^2\gamma + n_e^2\sin^2\gamma)\sin\psi_x}{\sqrt{n_o^2 - \sin^2\psi_x}} = 0 \qquad (2.11)$$

This equation is independent of film thickness and therefore the tilted angle of the optic axis can be obtained by substituting the measured ψ_x into equation (2.11). The method to obtain ψ_x is to examine the transmittance variation as a function of incident angle. Here ψ_x is defined as the incident angle where the retardance achieves a local maximum. A typical transmittance variation is shown in Fig.2-9, where the simulated results of a 50-μm-thick nematic LC with γ =5°, n_e=1.74, n_o=1.55, and λ =632.8 nm are presented. The symmetry point ψ_x of the transmittance curve corresponds to the maximum of optical retardance (δ).

The maximum δ occurs at an angular position where the angle between incident direction and optic axis is θ=90°. At this direction, $n_{eff}(\theta) = n_e$. The phase retardation becomes maximal and is independent of sample thickness.

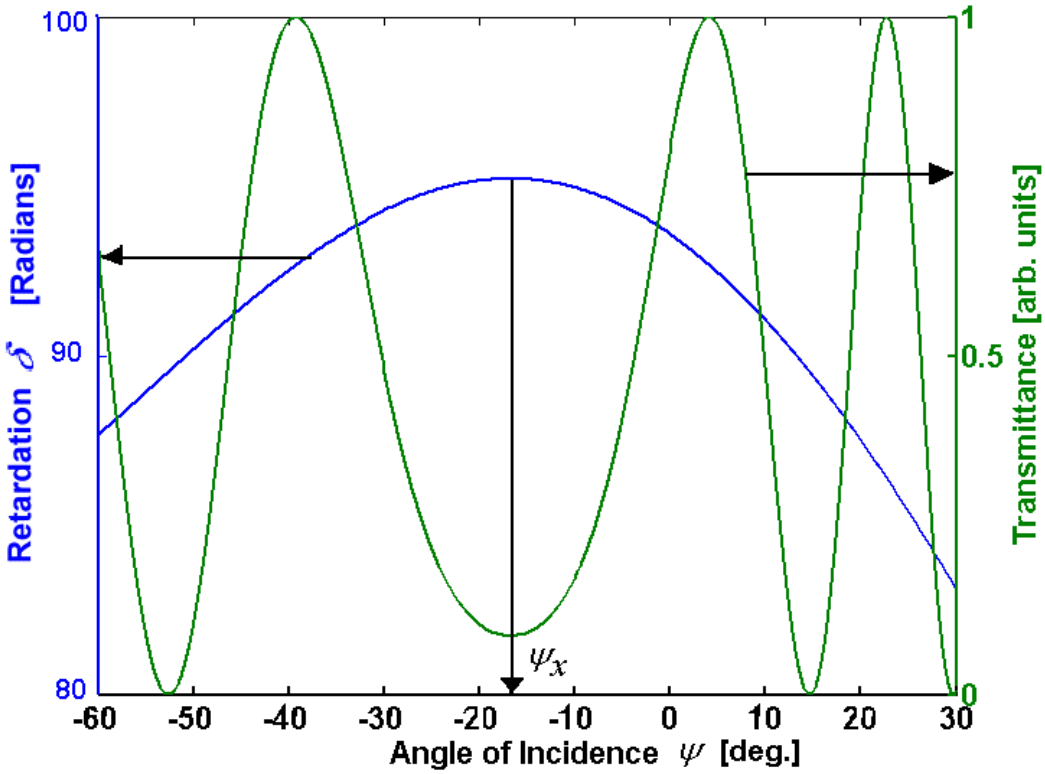

Fig.2-9 Angular dependence of optical phase retardation δ and transmittance for a 50-μm-thick nematic LC layer with γ =5°, n_e=1.74, n_o=1.55, and λ =632.8 nm. The symmetry point ψ_x on the transmittance curve corresponds to the maximum of the δ curve.

According to the simulated results shown in Fig. 2-9, we also find some limitations of this technique. When pretilt angle (γ) increases, ψ_x will eventually exceed the measurable range (see Fig.2-10), where the accurate determination of ψ_x becomes impossible. The measurable range of pretilt angle lies either below 20° or higher than 80°. In other words, the technique can not be employed to measure sample with tilt angle lying within 20°≤ γ ≤80 [2]. Although in reference [4] an extended crystal rotation method was proposed to solve the problem. Some limitations as discuss in Chapter 1 remain.

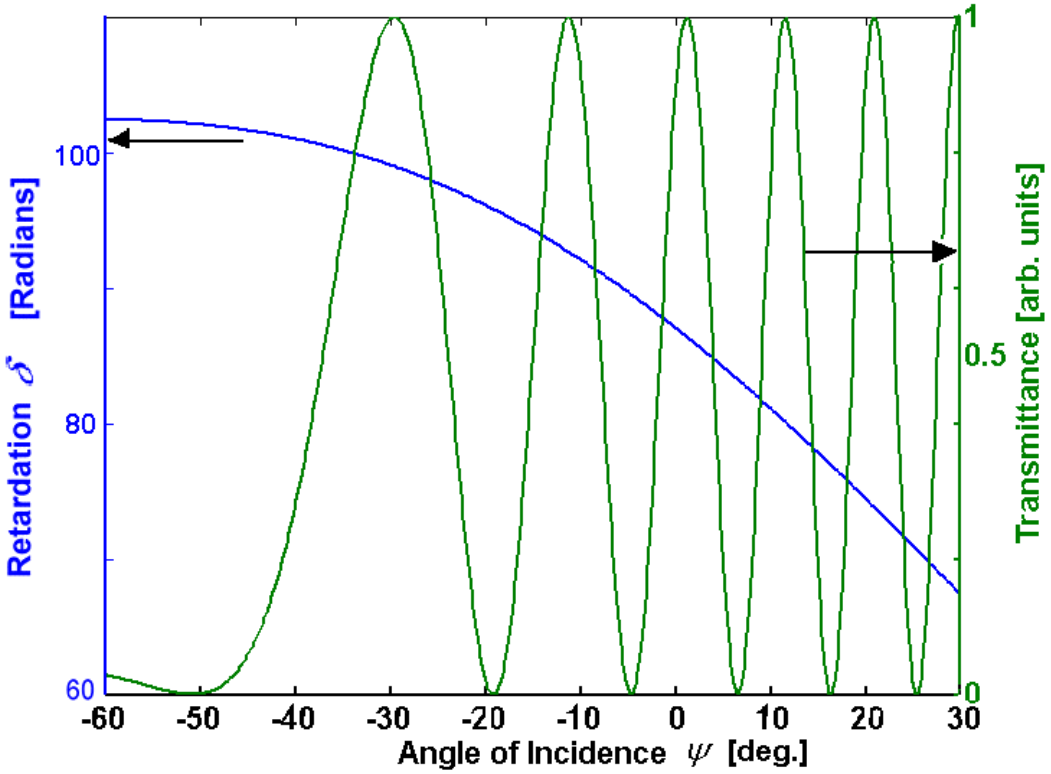

Fig.2-10 Angular dependence of optical phase retardation δ and transmittance for a 50-μm-thick nematic LC layer with γ =15°, n_e=1.74, n_o=1.55, and λ =632.8 nm. The symmetry point ψ_x on the transmittance curve exceeds the max.value of achievable angle of incidence.

Method to Obtain Polar Angle and Film Thickness by Using Curve Fitting Technique

Curve fitting technique can be employed to α and h by fitting the measured optical transmittance curve to Eq.(2.9). The method is applicable for any value of α. Let's take 50-μm-thick nematic LC layer with γ =15° as an example. A curve with 21 data points were extracted from ψ = 0° to ψ = –60°. We can observe that the curve is not symmetric. With the known n_e and n_o and proper initial values of thickness and polar angle, we fit the curve to Eq.(2.9). The fitting result is shown by the blue curve shown in Fig.2-11, which

yields a film thickness of 51.6 μm and polar angle of 14.8°, which are near to the exact values used. The slight difference can be further reduced by using better initial guess or a smaller fitting error criterion.

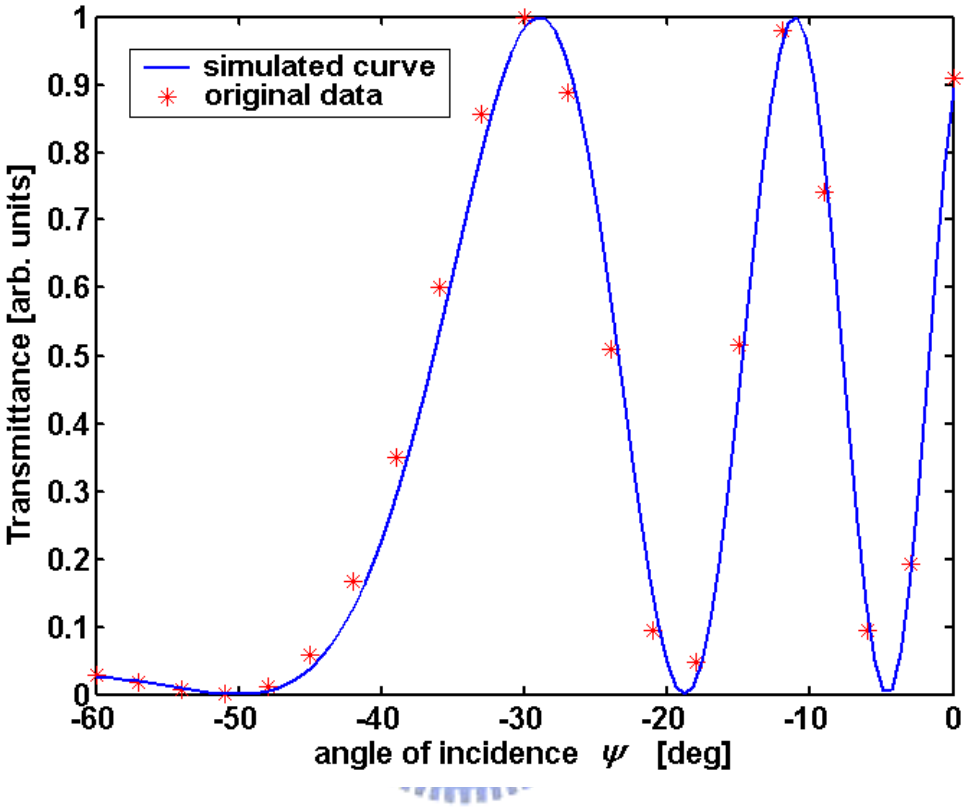

Fig . 2-11 For a 50- μm-thick nematic layer with γ=15°, the simulated result is γ=14.8° and thickness = 51.6 μm .

2-3 Image Data-Taking Procedure

2-3-1 Compensation of the Reduced Images

By using a rotating sample scheme, we may encounter difficulty when sample thickness is large. The major problem can be from the images from different incident angles may not overlap with each other at pixel-by-pixel level. This problem can be solved as follows:

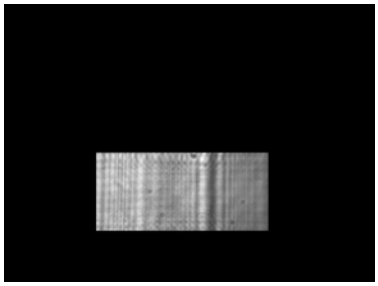

(a) Normal incidence

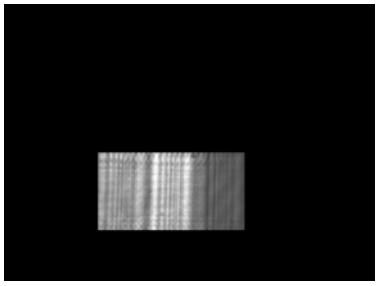

(b) reduced image from oblique incidence

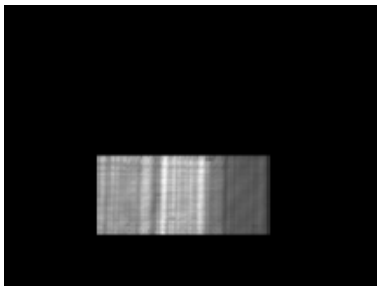

(c) Compensated image of oblique incidence

Fig.2-12 (a) Image taken at normal incidence ($\psi = 0°$); (b) reduced image size from oblique incidence ($\psi \neq 0°$); (c) compensated image of oblique incidence

With normal incidence ($\psi = 0°$), the projected area of sample onto CCD is largest (see Fig.2-12(a)). By increasing the incident angle ψ, the projected area on CCD becomes smaller (see Fig.2-12(b)). Oblique incidence not only reduces the image size but also shift image from the center of CCD.

Due to the sample rotation along y-axis, both the size reduction and spatial shift occur along x-axis. To remove the effect of spatial shifting, we first use the image boundary taken at normal incidence as a reference. We then employ a linear interpolation procedure to transform the reduced image size at oblique incidence back to the normal-incidence dimension, as shown in Fig.2-12(c).

In an actual measurement, we attach an adjustable slit or aperture on the front surface of the specimen. Therefore, imaging processing software can clearly detect the boundary between noise and signal.

In Fig.2-13, the x-axis is the pixel position along the x-axis of Fig.2-12, and y-axis is

the light intensity. It presents one-dimensional slices of the images taken at normal incidence, oblique incidence without size recovery, and oblique incidence with size recovery. After such a cautious procedure, we can reliably remove the image distortion originating from the influences of finite thickness and oblique beam incidence.

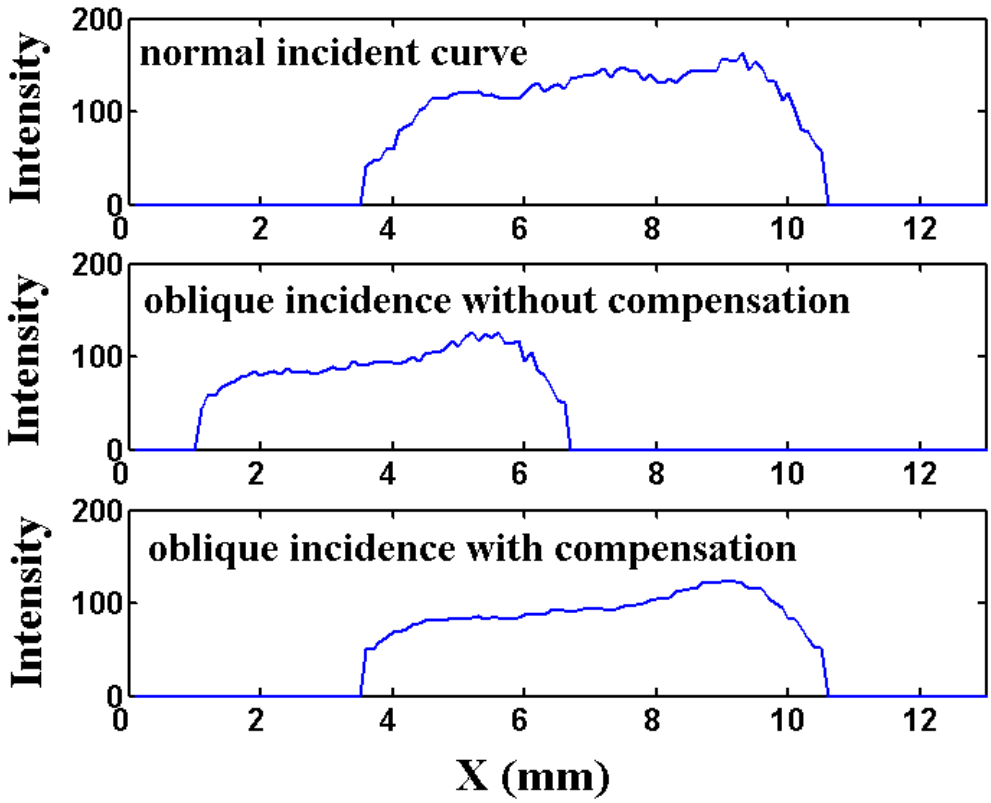

Fig .2-13 One-dimensional slice of images takes at (a) normal incidence ($\psi = 0°$), (b) oblique incidence with $\psi \neq 0°$ (c) oblique incidence with image interpolation

2-3-2 Removal of Interference Pattern by Means of Fast Fourier Transform (FFT) Filtering Procedure

The images captured from CCD are often affected by interference pattern originating from multiple-beam reflection between two interfaces of specimen. There could be several interference patterns along various directions with different spatial frequencies. The interference effect not only affected imaging polarimeter but also single-point

measurement apparatus. Fortunately, this interference pattern can be removed by fast Fourier transform (FFT) filtering technique.

Fig. 2-14(a) shows an image of $LiNbO_3$ wafer, which exhibits three sets of interference patterns along three directions (horizontal, vertical and slant). After processing with FFT, Fig.2-14(b) presents the resulting spatial frequency map. We filter out the corresponding interference patterns by removing these high spatial frequency components as shown in Fig.2-14(c). Finally, an inverse Fourier transform of (c) is performed and the resulting image is presented in Fig.2-14(d). We can observe the interference patterns disappear completely. Here we remove these high spatial frequency components by setting these values as zero. Therefore, the steep change in frequency domain will produce ripple near image's edge after inverse Fourier transform. And this ripple will be eliminated by other graphic software. Another way to filtering was to replace interference components in frequency domain with average value, not with zero.

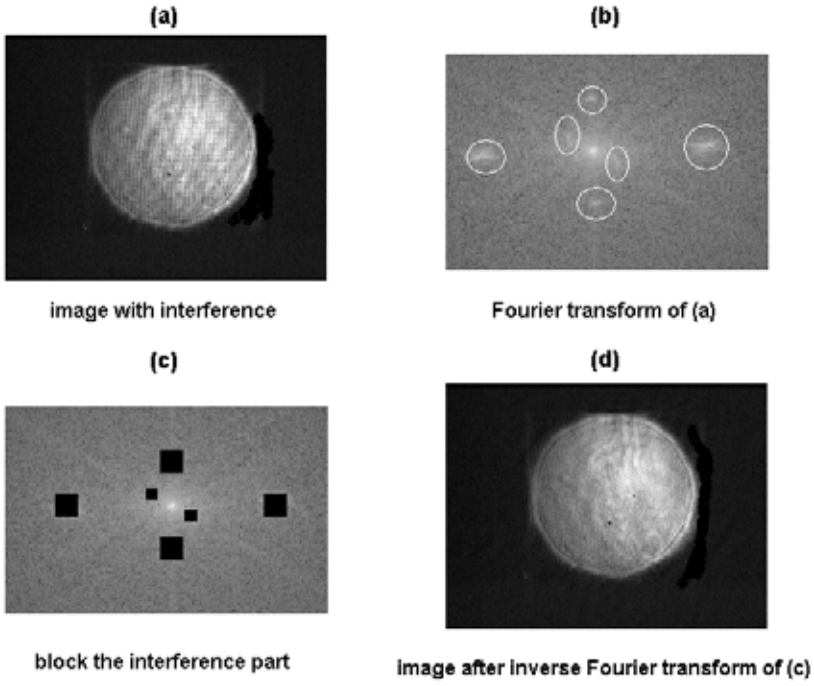

Fig .2-14 (a), Image contaminated with interference patterns (b), Fourier transform of (a); (c) the spatial frequency components to be removed; (d) image obtained by inverse Fourier transform of (c)

After presenting our theory and the principle of measurement, we applied our technique on three samples in order to show the applicability and usefulness of the imaging polarimetry. The first sample is a 1.1-mm thick $LiNbO_3$ single crystal wafer. The second specimen is a 4.9-μm thick home-made liquid crystal cell, and the third specimen is a commercial liquid crystal spatial light modulator (SLM).

2-4 Feasibility Study

2-4-1 $LiNbO_3$ Wafer

To demonstrate the functionality of the proposed method, we first apply our apparatus on a 1.1-mm thick z-cut stoichiometric $LiNbO_3$ single crystal wafer with indices of refraction of n_e=2.204 and n_o=2.296. The crystal was grown from a high temperature melt of Li_2O, K_2O, and Nb_2O_3 with appropriate molar ratio [10]. The UV absorption edge and Curie temperature measurements indicate the $LiNbO_3$ single crystal is indeed stoichiometric [11].

The optic axis of this wafer is along the surface normal of the crystal which yields a polar angle of α=0°. Since the optic axis is along z direction, the specimen is rotated about y-axis for 4 degrees toward x direction. The analyzer is rotated to vary ϕ from 0° to 180°. Nineteen pictures can be obtained by taking images with CCD every 10°. From the nineteen images, a curve of 19 data points for each pixel is collected and is fitted to Eq.(2.4) to deduceβ. Fig.2-15 is the 2-dimentional distribution of the azimuthal angle β of the z-cut $LiNbO_3$ single crystal specimen.

Fig.2-15 A map of the azimuthal angle of the optic axis of a tilted z-cut $LiNbO_3$ wafer

From Fig.2-15, the azimuthal angle is not zero. Four possible reasons may cause such a deviation:

1) Incomplete removal of multiple-beam interference patterns;
2) The CCD used in this study possesses only 256 levels (8 bit) with limited resolution;
3) The non-uniformity of optics used, particularly for analyzer;
4) Dust or small particle stick on optics which can scatter the incident light.

To assess the measurement precision of optical retardance with our system, we measure the optical retardance by rotating the analyzer but without inserting any birefringent sample. The histogram of the measured two-dimensional distribution of δ is presented Fig.2-16. The histogram peaks at δ =0.175 rad. with a full-width-at half-maximum (FWHM) of 0.016 radian. Therefore we estimate the precision to be about $0.0175\times180/\pi \cong 1$ degree.

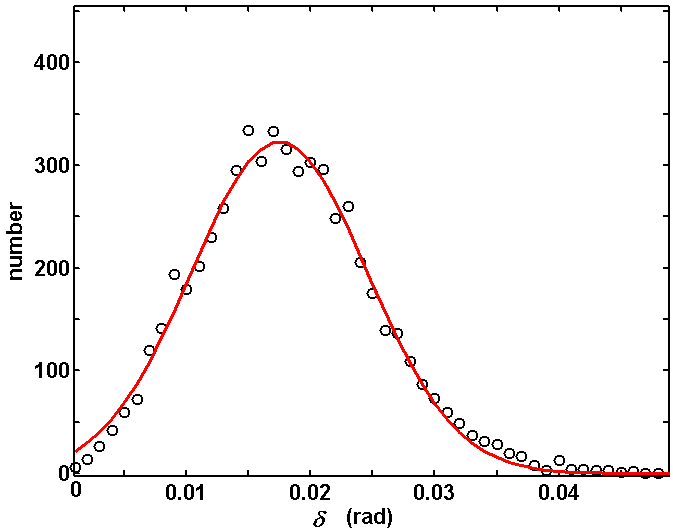

Fig.2-16 Histogram of δ image without sample. The peak occurs at 0.175 rad. With a FWHM of 0.016 rad.

We proceed to estimate the resolution of azimuthal angle measurement. We use $LiNbO_3$ as a standard sample whose optic axis is known to along z-direction uniformly. All data in Fig.2-15 are analyzed and is presented in histogram (Fig. 2-17). It can be seen that β peaks at 1.7^o with a full-width-at half-maximum (FWHM) of 4.1^o. The reason that the peak does not occur at zero could be caused by the sample not tilted exactly along x direction.

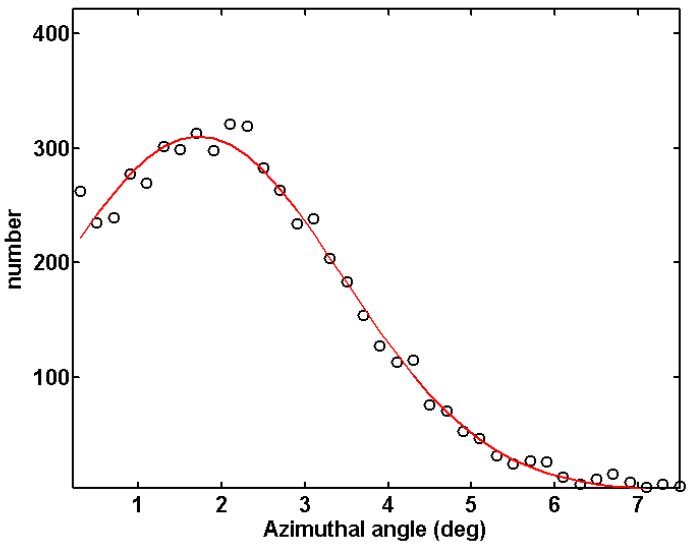

Fig .2-17 Histogram plot of Fig.2-15.

We then fix ϕ to be $\pi/4$ and let $\sin 2(\phi-\beta)$=1 in Eq.(2.4). The wafer is rotated with the y-axis as the rotation axis to vary incident angle ψ. Fig.2-18 shows calculated results with α =0° and the thickness *h* changing from 1.1 mm to 10 mm and ψ from -10 degrees to +10 degrees. This diagram reveals that to measure a specimen with thickness ranging from 1 mm to 10 mm, 21 images should be collected by taking one CCD exposure per 1° from ψ= -10° to +10°.

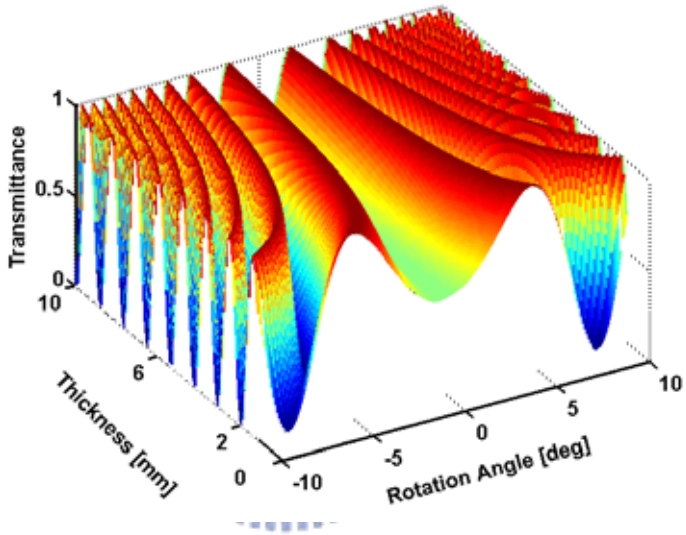

Fig .2-18 Calculated optical transmittance of uniaxial film with n_o=2.296; n_e=2.204, α =0° and thickness varying from 1.1 mm to 10 mm

During measurement, we attach an aperture with a 0.8 cm diameter onto the front surface of sample to define the imaging area. The computer software will search each diagram for the area with signal larger than background noise. To reduce the memory requirement, each picture is averaged with a format of 3×3 pixels to yield an image of 160×213 pixels.

We use the circular boundary at ψ= 0° as a standard and transform the images with oblique incidence to its original size. From the 21 pictures, the intensity variations corresponding to each pixel are assembled and fit to equation to deduce the two-dimensional distributions of film thickness *h* and polar angle α of the optic axis.

The measured optical transmittance curves are similar to that depicted in Fig.2-18. The calculated results with thickness to be 1.14 mm are shown in Fig.2-19(a), where the green curve denotes the optical retardation and blue line is optical transmittance. Fig.2-19(b) shows the experimental results from a specific pixel. The red circles are experimental data, and blue line is the fitting curve.

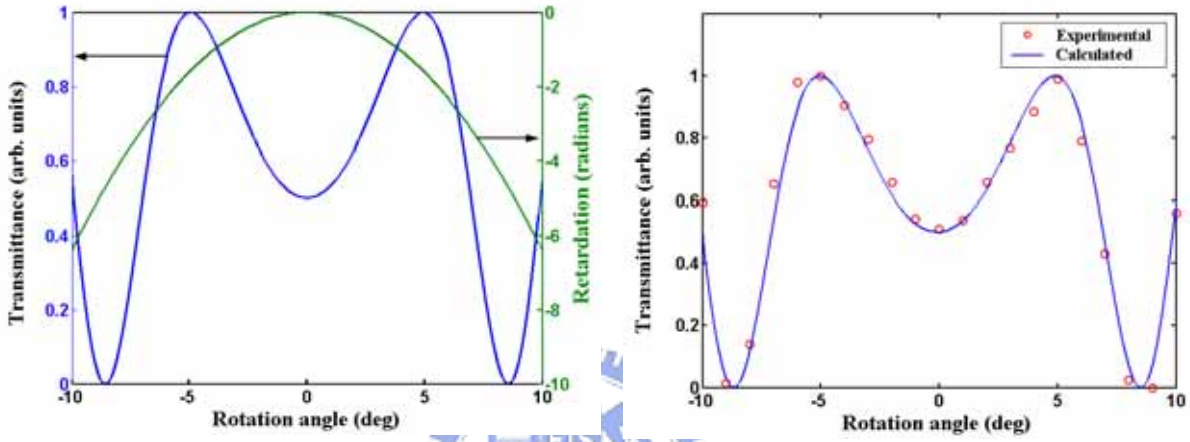

(a) (b)

Fig .2-19 (a) Calculated curves of optical transmittance and retardance of a uniaxial film with n_o=2.296; n_e=2.204, α =0° and thickness 1.14 mm. (b) Measured and fitting curves of optical transmittance of a $LiNbO_3$ wafer.

After curve-fitting to the optical transmittance curves from 10,000 pixels, the two dimensional distributions of the thickness and the pretilt angle can be obtained, which are presented in Fig.2-20.

The $LiNbO_3$ wafer used is a stoichiometric $LiNbO_3$ grown from a high temperature solution of Li_2O, K_2O, and Nb_2O_3 with a seed. The results with present method prove that the optic axis of the single crystal wafer is along to the z-axis and the distribution of the optic axis is very uniform (<0.05) over the measured area. The deviation from z-axis at the boundary is slightly larger than that at the center, which could originate from an influence of the seed position during the crystal growth.

The histogram of polar angle is shown in Fig.2-21(a). It can be seen that α peaks at 0.02^{o} with a full-width-at half-maximum (FWHM) of 0.06^{o}. The precision of polar angle measurement is better than that of azimuthal angle. The histogram of thickness distribution is presented in Fig.2-21(b). It is shown that thickness distribution peaks at 1.145 mm with a FWHM of 0.025 mm.

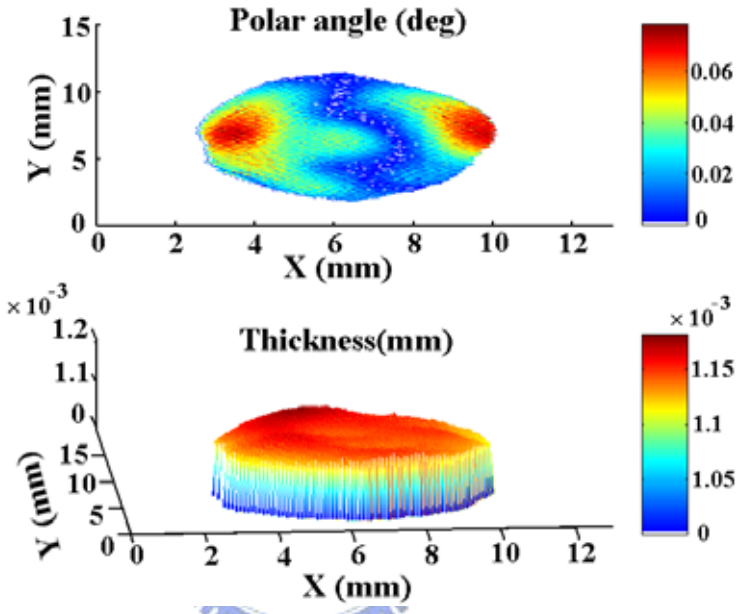

Fig .2-20 Two-dimensional distributions of the polar angle of the optic axis and the $LiNbO_3$ wafer thickness.

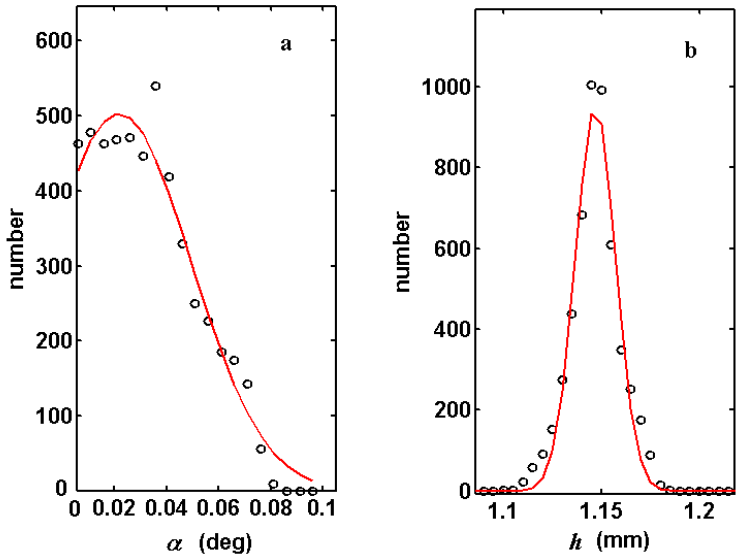

Fig .2-21 (a) Histogram of the polar angle; (b) histogram of the thickness shown in Fig. 2-20

2-4-2 Home-made liquid crystal device

To ensure the current polarimeter is also suited for thin sample, we prepared a vertical-alignment liquid crystal cell with a thickness of 4.9 μm and n_e=1.4756 and n_0=1.5586.

The minimum phase retardation of the vertical-alignment LC cell occurs at zero applied voltage. A measured curve of phase retardance as a function of applied voltage is presented in Fig.2-22. From this measurement, we can estimate the polar angle of the LC director to be ≅2° and thickness ≅4.9μm at zero voltage.

Fig.2-22 Measured phase retardance of a home-made liquid crystal cell as a function of applied voltage.

With the known values of n_e, n_o and h, we can also obtain a theoretical curve of phase retardation as a function of polar angle, which is shown in Fig.2-23. The calculated curve shows that phase retardance increases with the polar angle of LC director.

By comparing Fig.2-22 and Fig.2-23, we can determine that the polar angle of LC director for a given applied voltage. For example, the polar angle is about 2° at zero voltage, 30.78° at 3.3 VAC, and 49° at 4.6 VAC. We measured the polar angles with our

polarimetric technique and found the results agree very well with the predict values.

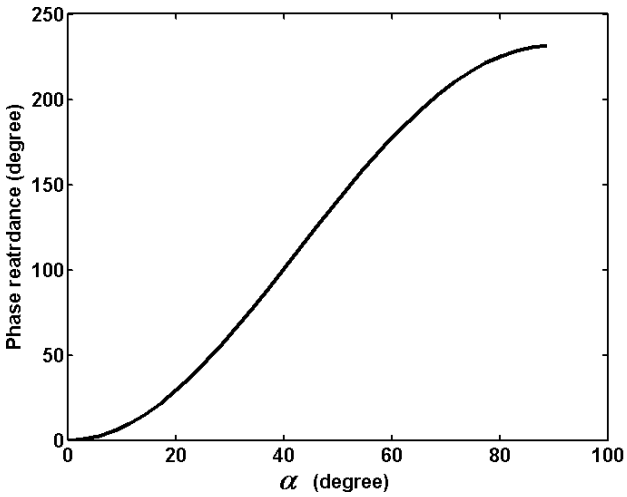

Fig.2-23 Phase retardance of a home-made liquid crystal as a function of polar angle.

• Measurement results with 4.6 VAC

We first perform an analyzer scan to deduce the angle β of the LC device, which also reflects the rubbing direction of the liquid crystal cell. We align the rubbing direction to be along with x axis to make β =0°.

The two-dimensional distribution of azimuthal angle of the LC director is plotted in Fig.2-24(a). The corresponding histogram of the β distribution peaks at 0° with an FWHM of 3.5°. The FWHM indicates the LC molecules align very well along the x-axis and generates a high optical contrast.

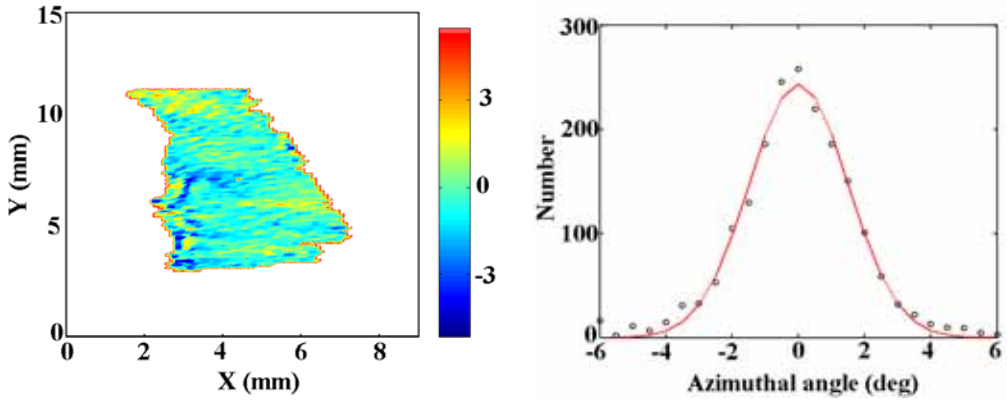

(a) **(b)**

Fig. 2-24. An in-plane distribution of the azimuthal angle of LC director of the home-made LC cell taken at an applied voltage of ±4.6 V VAC @ 1-kHz.

We then proceed to the next step to deduce the polar angle α and film thickness h. This is done by first rotating the analyzer to $\phi=\pi/4$ to fulfill the condition of $\sin 2(\phi-\beta)=1$. Theoretical results of optical transmittance depicted by Eq.(2.9) with α =49°, film thickness h varying from 4.9 μm to 25 μm and ψ from –50 degrees to +50 degrees are presented in Fig.2-23. The diagram suggests that for a uniaxial film with thickness ranging from 4.9 μm to 25 μm, optical transmittance image shall be taken per 5° with ψ varying from –50° to +50°.

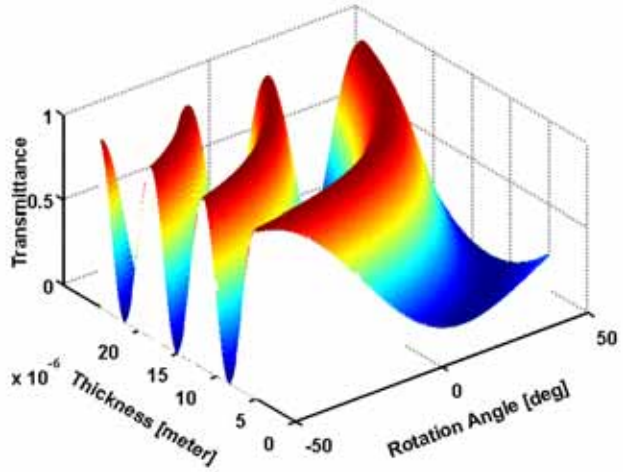

Fig .2-25 Calculated optical transmittance curves of a uniaxial film with n_o=1.5586; n_e=1.4756, α =49° and thickness varying from 4.9 μm

to 25 μm

Here we want to mention that the limit of thinner thickness in this proposed method was due to we require to normalize transmittance. Therefore, the variation of transmittance should have both maximum and minimum values. For thinner thickness to sub-micron level, the maximum and minimum values will not occur.

If we want to extend the measured range to thinner thickness, the absolute value of transmittance should be used. The difficulties was to consider reflection in Eq.(2.9). Here we used method was normalized transmittance.

A one-dimensional slice of Fig. 2-25 with a film thickness of 4.9 μm is presented in Fig.2-26(a). The green-colored curve denotes the optical retardation and the blue line is the optical transmittance. A measured curve of 21 data points can be assembled from the 21 images for each pixel. Fig.2-26b shows one of such measured curves and its fitting result of the liquid crystal cell at 4.6 VAC. Two-dimensional distributions of thickness and polar angle of LC director of the liquid crystal cell can be obtained by collecting the fitting results of 10,000 pixels (see Fig.2-27).

We can further analyze the two-dimensional distributions and present the results in histogram format. The histogram of the thickness distribution peaks at 4.99 μm with a FWHM of 0.08 μm. The FWHM value can be used to indicate that the liquid crystal cell has a 0.1 μm variation in the thickness, which is roughly equal to the surface roughness of the ITO glass used. The polar angle of the liquid crystal molecule under 4.6 VAC voltage is about 48~49 degrees, which agrees with the theory very well. By combining $\Delta\beta$(FWHM), $\Delta\alpha$(FWHM), and Δh(FWHM), these parameters form a convenient set to reflect in-plane inhomogeneity of LC devices and shall be useful for quality control of LC device fabrication.

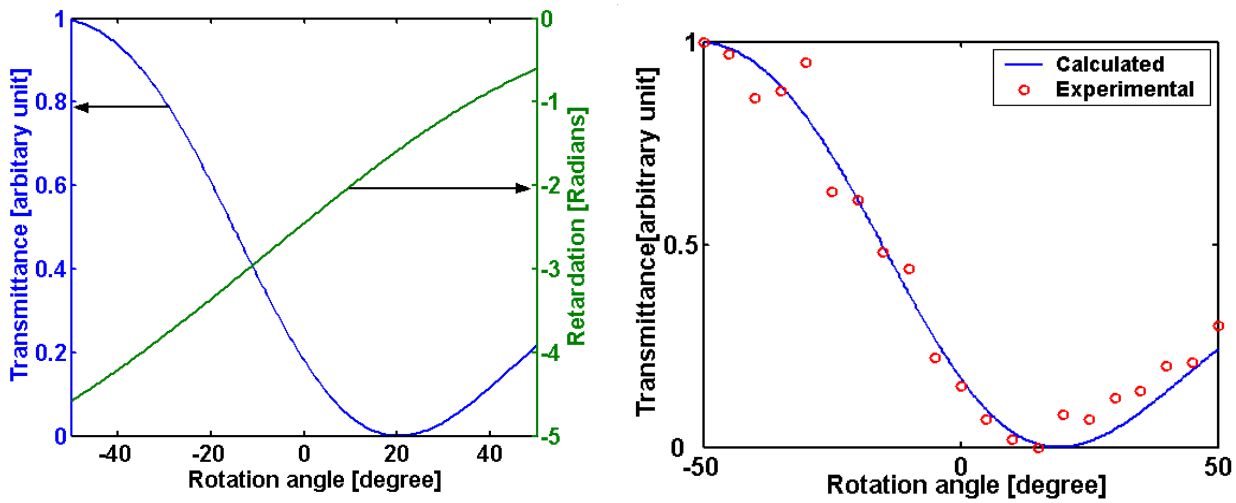

(a) (b)

Fig .2-26 (a) Calculated curves of optical transmittance and optical retardation of a uniaxial film with n_o=1.5586; n_e=1.4756, α =49° and thickness 4.9 μm, (b) Measured and calculated curves of optical transmittance of the liquid crystal cell at 4.6 VAC.

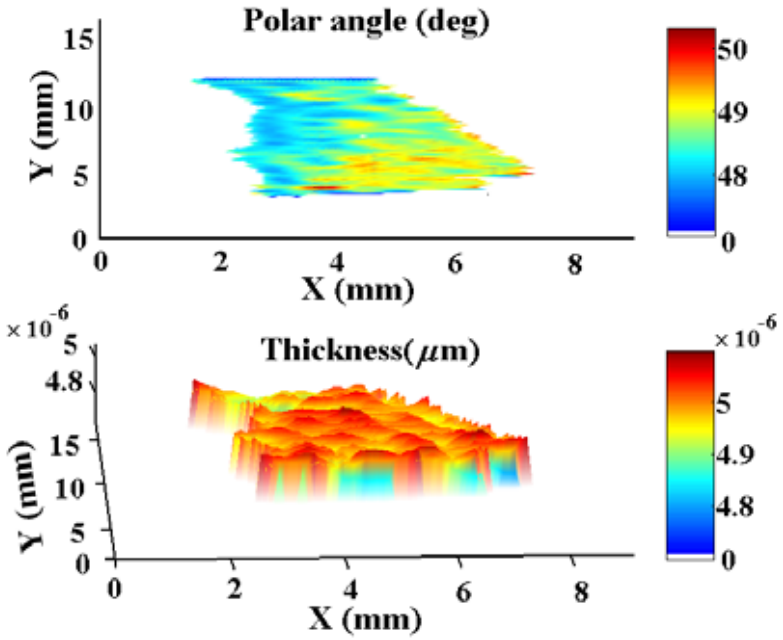

Fig .2-27 Two-dimensional distributions of the polar angle of the LC director (top) and the LC film thickness (bottom).

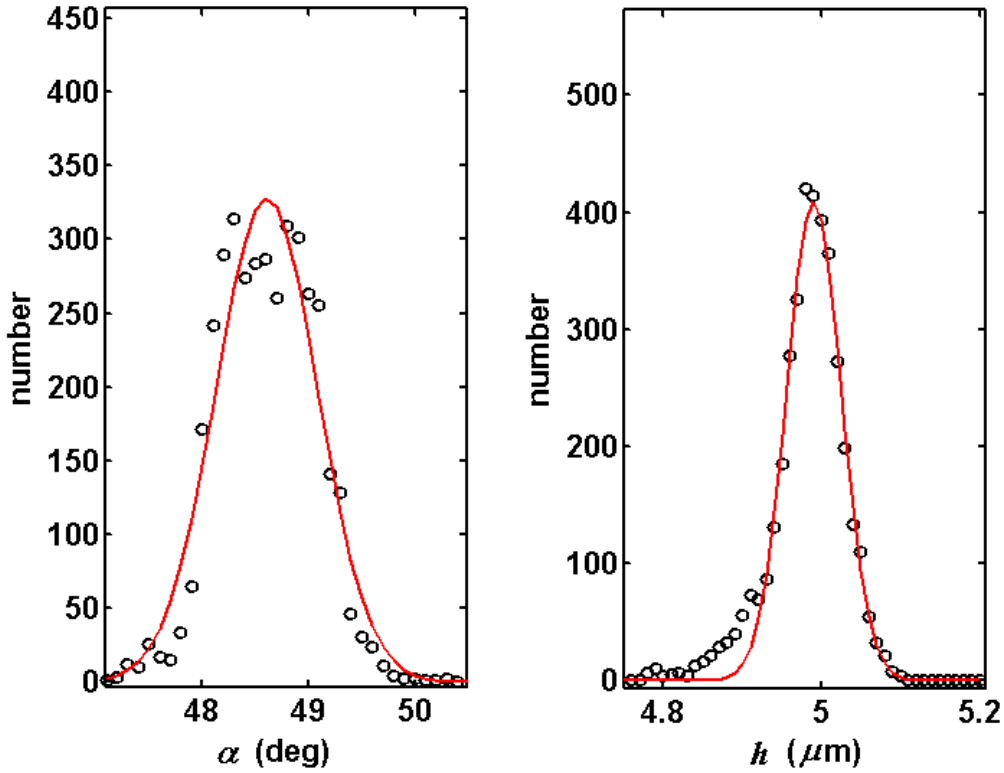

Fig .2-28 (a) Histogram of the polar angle of LC director, (b) histogram of the LC film thickness.

2-4-3 Spatial Light Modulator (SLM)

To further test the accuracy of our imaging polarimeter, we apply our apparatus on a commercial 1D liquid crystal spatial light modulator SLM-128 [12] from Cambridge Research and Instrumentation, Inc. The device is composed of 128 pixels with a pitch of 100 μm and a height of 2 mm. In one period, the pixel dimension is 97 μm separated by 3-μm gap. We group the 128 pixels into three collections and apply three different voltages of 2.44 V, 9.03 V, and 1.22 V from the left to right onto the three sets. The measuring procedures as detailed above are applied to the device and the results are presented in Fig.2-29. The LC film thickness is found to be 9.7 μm for all the three sets. The polar angle α however exhibits significantly different values of 53°, 20°, and 81°, respectively, reflecting clearly a field-induced tilt of LC director.

We further perform histogram analysis of Fig. 2-29. The results shown in Fig. 2-30 clear exhibit three peaks in the histogram of polar angle. But only one peak appears in the histogram of thickness distribution. The histogram of thickness peaks at 9.7μm with a FWHM of 0.09μm, which is also similar to the surface roughness of the ITO glass. Three peaks in polar angle correspond to 53°, 20.3° and 80.5° with FWHM of 1.2°, 0.5° and 1.08°, respectively. The slightly large FWHM widths at high polar angles (>50^{o}) are mainly caused by higher voltage sensitivity of the field-induced LC tilting at high tilted LC configuration. The measurement accuracy of polar angle is about 1 degree, which is mainly limited by the diffraction effect from the pixel pattern of SLM.

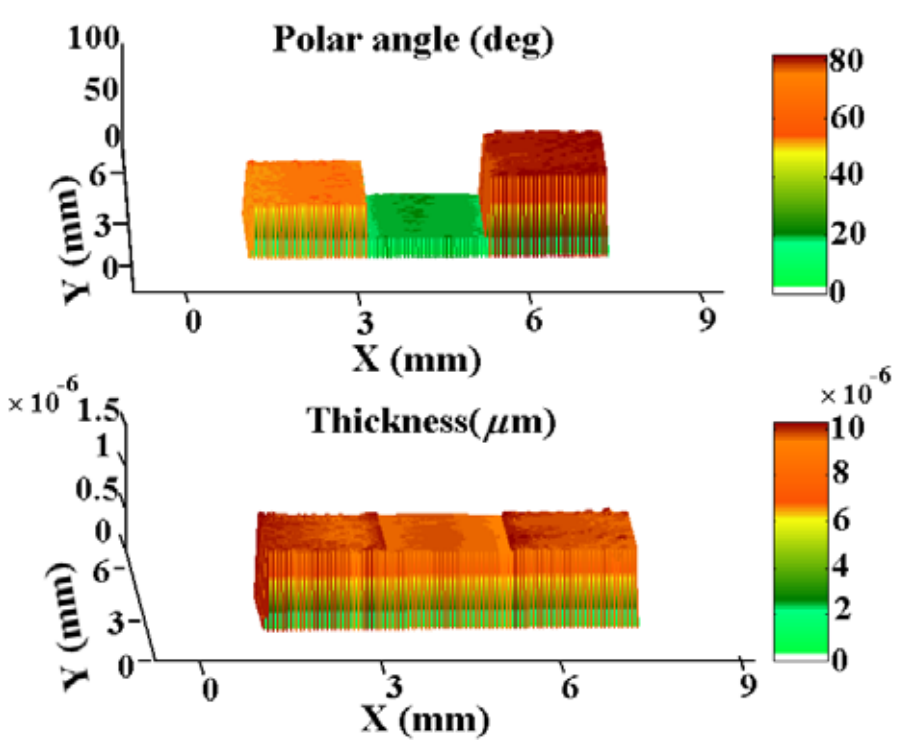

Fig .2-29 Two-dimensional distributions of the polar angle of the LC director and the LC film thickness of a LC spatial light modulator (SLM). The SLM is applied with a voltage of 2.44 V, 9.03 V, and 1.22 V (from the left to right), which yield a polar angle of α=53°,20° and 82°. The LC film thickness is about 9.7μm.

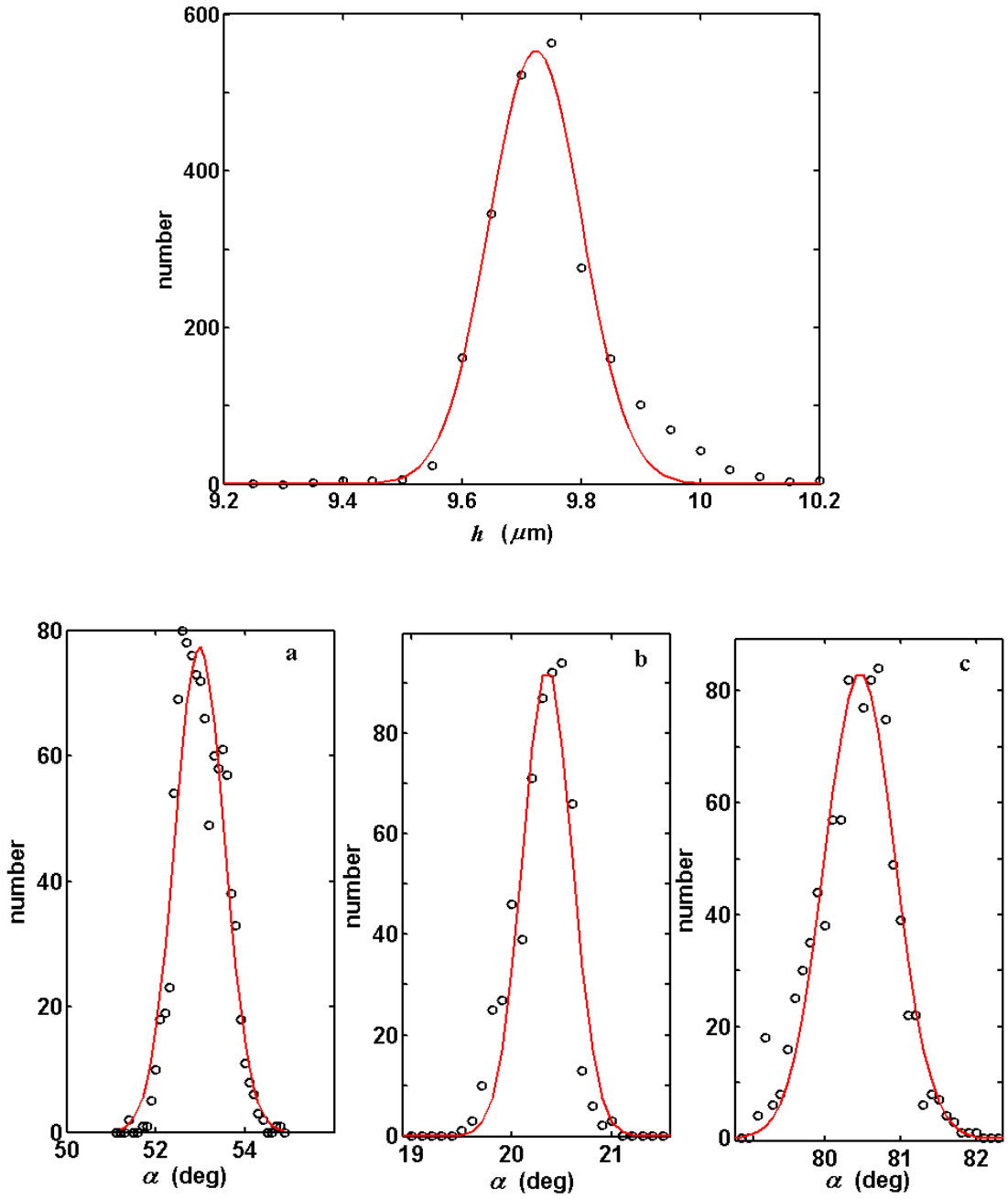

Fig .2-30 Histogram of SLM which is applied with a voltage of 2.44 V, 1.22 V, and 9.03 V. The three peaks in the histogram of polar angle correspond to α=53°, 20° and 82°.

Finally to summarize this chapter, we present an imaging polarimetry and related data taking procedure to yield the two-dimensional distributions of film thickness and optic axis orientation simultaneously. Three samples with different thickness were employed to test the functionality and usefulness of the technique. We demonstrate that

the distributions and the deduced parameters are of high value for quality control of liquid crystal display, optical crystal inspection, and biomedical inspection.

In contrast to the prior approaches, the current method uses a single apparatus to obtain both the thickness and the optic axis direction of optical crystals, so the cost can be effectively lowered. In addition, the present technique not only provides a convenient and effective measurement method but also overcomes several drawbacks encountered by many conventional polarizing measurement systems. The image procedure for removing the multiple-beam interference effect and image compensation for oblique incidence is devised. With these procedures, correctly overlapping images at pixel-by-pixel level can be achieved to yield an accurate measurement result. Our scheme can be employed for monitoring film thickness from 1 μm to mini-meters with an in-plane spatial resolution of better than 50 μm.

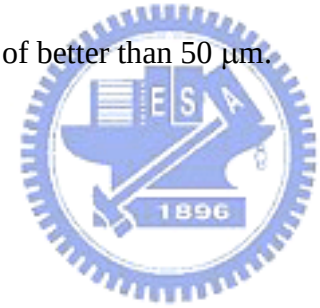

Chapter 3

Study on the Defect Structures of Nematic Liquid Crystal

In the previous chapter, we had successfully demonstrated our apparatus with a 1-mm thick $LiNbO_3$ wafer and 5 μm thick liquid crystal devices to ensure the principles, measurement precision, and functionalities involved. So in this chapter we shall proceed to employ this apparatus for studying defect structures of nematic liquid crystal on weakly anchoring alignment surface.

In nearly all electro-optic applications involving liquid crystals, it is necessary to uniformly orient the liquid crystal in a certain direction. Owing to its great importance in the fabrication of liquid crystal displays (LCDs), the topic has been intensely investigated [13]. Among these research efforts, the establishment of a rubbing-free LC alignment method is an important target due to the possibility of improving the production yield of LCDs and improved viewing angle. Previous studies of LC alignment on photopolymer substrates open a new possibility to control the LC alignment without a rubbing process [14], and these studies indicate that the photo-alignment (PA) method is the most attractive candidate as a future rubbing-free technique. PA method also gives us a new opportunity to investigate the LC alignment mechanism on polymer substrates due to its

well-controlled weak anchoring nature. In this chapter, we present a study of LC alignment on a photopolymer substrate with weak anchoring strength by using our imaging polarimetric technique.

3-1 Néel wall without point defect

The surface azimuthal anchoring energy is one of the effective parameter to reflect the strength of LC molecular alignment on a surface. The parameter indicates how much energy is required in order to deviate the azimuthal angle of LC director from the easy axes where it is anchored. Generally, the surface azimuthal anchoring energy given by the PA method is relatively weak comparing to a typical mechanical rubbing surface. The anchoring energy of a PA surface is controlled by varying the UV exposure. Many measurement methods of the azimuthal anchoring energy have been proposed during the past two decades. These measurement methods may be divided into two groups depending on whether an external perturbing field is applied (field-on techniques) or not (field-off technique) [15]. Néel wall method was categorized as field-off technique.

It is well known that the azimuthal anchoring energy of the sample can be estimated from the width of Néel wall [16]. Fig.3-1 depicts the arrangement of the LC directors around a Néel wall defect, where it is assumed that the z-axis is along the cell thickness, the LC molecules are oriented parallel to the glass surface (*i.e.*, the x-y plane), and ϕ(y) is the angle between the director and easy axis (x-axis).

3-1-1 Prediction of Theory

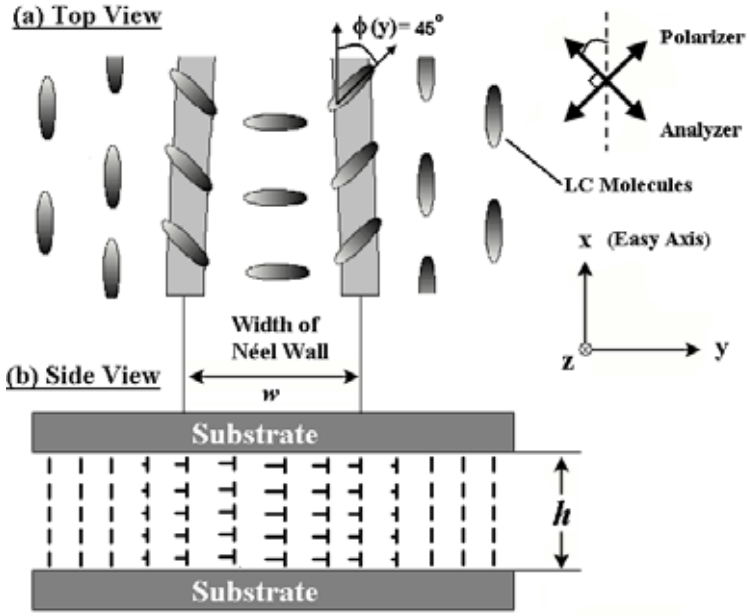

Fig .3-1 The LC configuration near a Néel Wall* defect. *The azimuthal anchoring energy could be estimated by the measurement of the width of the Néel Wall w.

Here we assume the direction of the easy axes on both substrate surfaces to be along the x-direction, and all the LC molecules to be oriented parallel to the cell surface (*i.e.*, no LC pretilt).

With this coordinate system and by substituting LC director n = (cos(ϕ(y)), sin(ϕ(y)), 0) into Frank's elastic theory of nematic liquid crystal, the bulk elastic free energy density can be derived to be [17].

$$f_{elas} = \frac{1}{2} K_{11} \left(1 + \frac{K_{33} - K_{11}}{K_{11}} \sin^2 \phi \right) \left(\frac{\mathbf{d}\phi}{\mathbf{d}y} \right)^2 . \qquad (3.1)$$

The total free energy along the y-axis is given by

$$F = \int_{-\infty}^{\infty} h \cdot f_{elas} \mathrm{d}y + \int_{-\infty}^{\infty} A_{\phi} \sin^2 \phi \mathrm{d}y,$$

where A_{ϕ} is the azimuthal anchoring energy and h denotes the cell gap.

By minimizing the total free energy with respect to ϕ, we obtain

$$\frac{\mathbf{d}F}{\mathbf{d}y} = h \cdot f_{elas} + A_\phi \sin^2 \phi = 0$$

$$\Rightarrow \frac{\mathbf{d}\phi}{\mathbf{d}y} = -\sqrt{\frac{2A_\phi}{h \cdot K_{11}}} \cdot \sin\phi,$$

where the elastic constants are assumed to be $K_{11} \approx K_{33}$. So the above equation can be integrated to yield

$$y(\phi) = -\frac{\xi}{2} \ln\left(\frac{1-\cos\phi}{1+\cos\phi}\right),$$

where ξ is a characteristic length which is given by $\xi = \sqrt{\frac{h \cdot K_{11}}{2A_\phi}}$.

From Eq.(3.2), it is easily found that

$$y(90°) = 0$$

$$y(45°) = -\frac{\xi}{2} \ln(3 - 2\sqrt{2}).$$

The width of the Néel wall w corresponds to $w = y(45°) - y(-45°) = 2(y(45°) - y(0°))$; therefore,

$$w = -\ln(3 - 2\sqrt{2}) \sqrt{\frac{h \cdot K_{11}}{2A_\phi}}. \qquad (3.2)$$

Finally, a relationship between w and A_ϕ can be found:

$$A_\phi = \frac{\left[-\ln(3 - 2\sqrt{2})\right]^2 h \cdot K_{11}}{2w^2}. \qquad (3.3)$$

We can further approximate $\left[-\ln(3 - 2\sqrt{2})\right]^2 / 2 \cong 1.5536$ to be about 2 [16].

By using Eq. (3.2), we can note that anchoring energy is inverse proportion to the square of the ***Néel Wall*** width.

3-1-2 Experimental Observation

To observe alignment defects in LC, we insert a magnifying lens to enlarge the image of defects. The LC we used was MLC2024 with n_e=1.5469 and n_o=1.4726. The LC cell spacer was 10 μm. An alignment film of PI-1349 was spin-coated on ITO substrates. We exposed the PI-coated substrates to a linearly polarized UV (LPUV) light. Total exposure energy was controlled by varying the exposure time. MLC2024 LC material was injected into the cell in an isotropic phase by heating it to 80°C to avoid the effect of flow alignment. After LC being injected, the cell was slowly cooled to room temperature. We inserted the LC cell between crossed polarizers and the resulting optical transmittance image is shown in fig3-2(a). Two long dark lines are observed and indicate the Néel wall. Fig.3-2(b) shows the configuration of LC director deduced from our imaging polarimetric setup. The directors of LC inside the dark lines are parallel to polarizer or analyzer (i.e. β =45° or 135°). We can also find that the LC directors being rotated 180 degrees across the Néel wall as predicted by the theory. The image we captured with CCD exhibits some interference fringes caused by multiple-beam reflection between two interfaces of the LC cell. This diffraction ring and interference pattern can be easily removed by fast Fourier transform (FFT) filtering technique. From the director distribution across the Néel wall, we can clearly show that the lateral resolution to be better than 50 μm.

By using Eq. (3-2), we measure the Néel wall's width is about w~90 μm. By substituting in Eq. (3-3), we can determine the azimuthal anchoring energy.

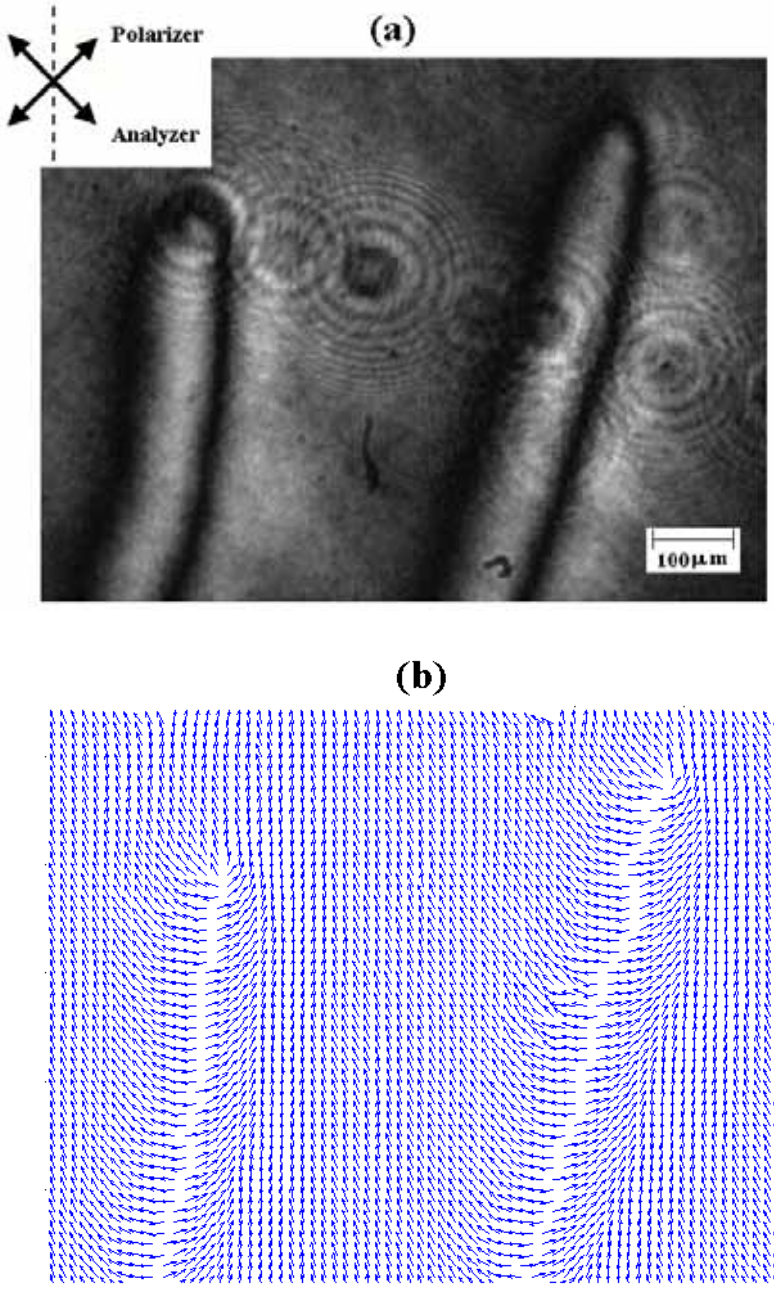

Fig . 3-2 (a) The image of a Néel Wall under crossed polarizers; (b) director configuration around the Néel Wall with wall width w~90 μm.

The measurement of surface anchoring energy with the wall method is possible for LC samples with cell thickness smaller than a characteristic length, *i.e.*, the so-called extrapolation length [18], b~$2K/W_s$. Here W_s is the total surface anchoring energy which

includes azimuthal anchoring energy and polar anchoring energy. For an alignment film with an extremely strong anchoring energy (W_s~1 erg/cm^2), *b* is of the order 100Å. If we have a film with a small value of W_s (~10^{-4} erg/cm^2), *b*~100 μm. If LC thickness is smaller than the extrapolation length, it is impossible to have any deviation in the LC director across the thickness ($\partial/\partial z \sim 0$).

The appearance of Néel wall defect reflects a weakness of the LC anchoring with a deformation of the LC director across the film thickness ($\partial/\partial z \sim 0$). Therefore Néel Wall could be stabilized along z direction, and director deformation allows only on the x-y plane. The thickness of our sample is about 10 μm which is smaller than a typical extrapolation length and satisfies the condition $\partial/\partial z \sim 0$.

Although $\partial/\partial z \sim 0$ indicates polar angle shall be constant along z direction, there is not forbidden to change on the x-y plane. For a homogeneously aligned cell, the LC directors lie on the substrates with $\alpha \sim \pi/2$. We observed the optical retardance changing across the Néel Wall. (see Fig.3-3(c))。 There are two possible causes to change optical retardation. First, it is due to a change of thickness and the second it could originate from a change of polar angle. Since a change in cell thickness is not allowed, we therefore attribute the variation of optical retardation to be from a variation in polar angle.

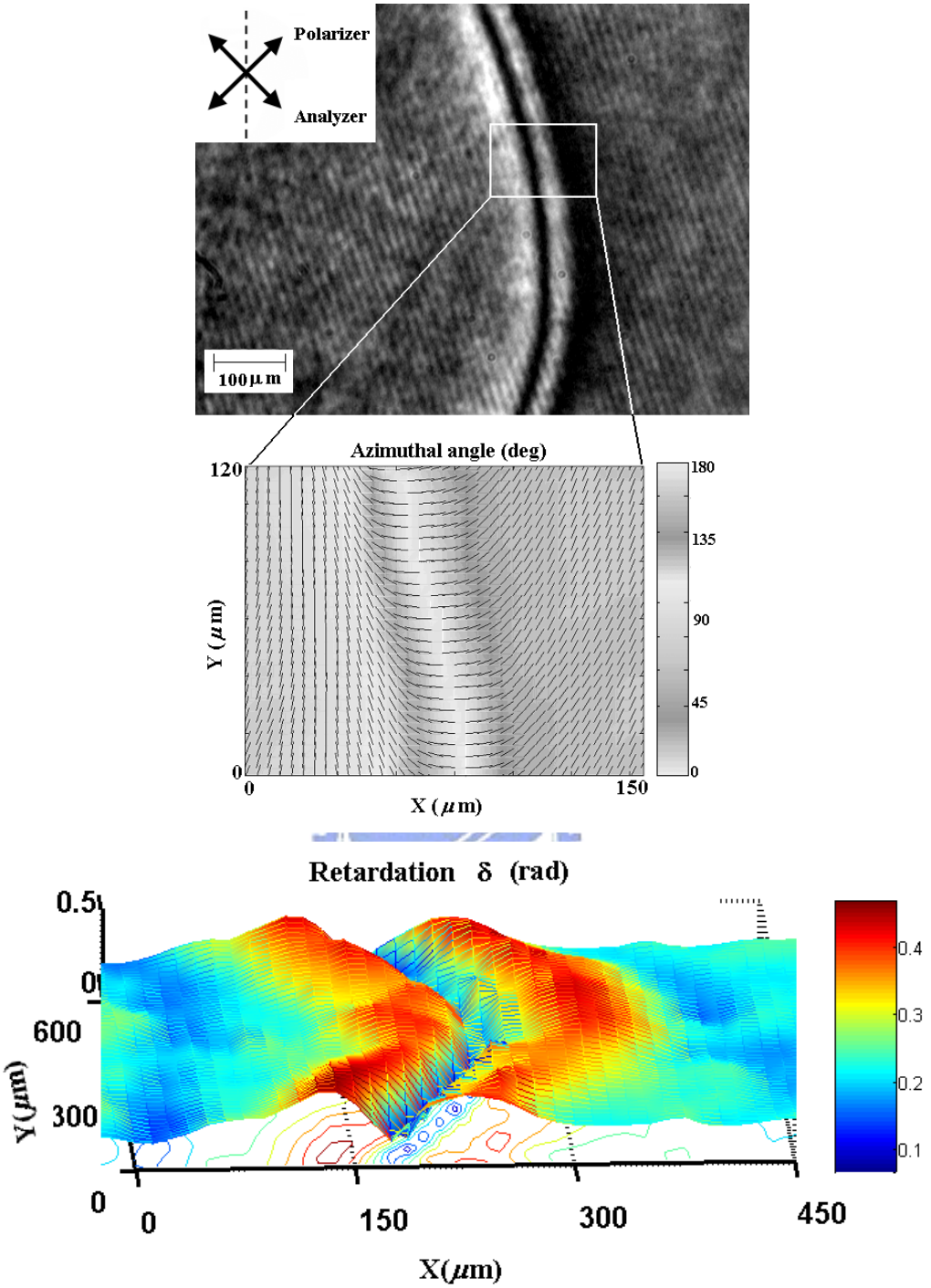

Fig.3-3 (a) The Néel Wall image taken with crossed polarizers; (b) LC director configuration around the Néel Wall; (c) 3D plot of the optical retardation across the Neel wall defect.

From Fig.3-3(c), we find that the change of phase retardation is perpendicular to Néel wall. Far from the Néel wall defect, the variation becomes small, which indicates the distribution of polar angle is uniform.

We attribute the variation of optical retardation to be from a variation in polar angle. To confirm the theory, we take a 1D slice along the x-axis from Fig.3-3(b) and (c) and the resulting profiles are presented in Fig.3-4. Fig.3-4(a) is the 1-D profile of optical retardance and (b) is the 1-D profile of azimuthal angle. The azimuthal angle of LC director has been added 45 degrees because of the easy-axis of the anchoring is along the y-axis.

It can be seen that far from left wall, retardation is about 0.2 radian and close to the left wall, retardation increases to 0.45 radian and then on the right it decreases to 0.2 radian at the center of walls where the LC director is perpendicular to the easy axis. When approaching to another wall, optical retardation increases to 0.45 radian again and finally decreases to 0.2 radian when far from the right wall. The variation of optical retardation is about $\Delta\delta \approx 0.25$ radian. We take this value in Eq. (2.7) and Eq. (2.8) and estimate the wall thickness to be about 10 μm. Under an assumption that 0.2 radian of the optical retardation, which corresponds to 80 degree of polar angle, the variation of retardation $\Delta\delta \approx 0.25$ rad shall correspond to a variation of polar angle $\Delta\alpha \approx 10°$. Therefore, we offer a picture of the LC director configuration in the following: At the far left side of the wall, the polar angle is about 80 degrees and near the left wall, polar angle increase to 90 degrees and then decrease to 80 degrees at the center of the Neel wall. When approaching to the right wall, polar angle increases again to 90 degrees, and finally decreases to 80 degrees when far from the right wall. That is to say that the polar angle of LC director is about 80 degree when the LC director is parallel or perpendicular to the easy direction and the polar angle becomes 90 degree when director is at both walls. This phenomenon may be caused by a compression force on LC molecules when LC

molecules are rotated.

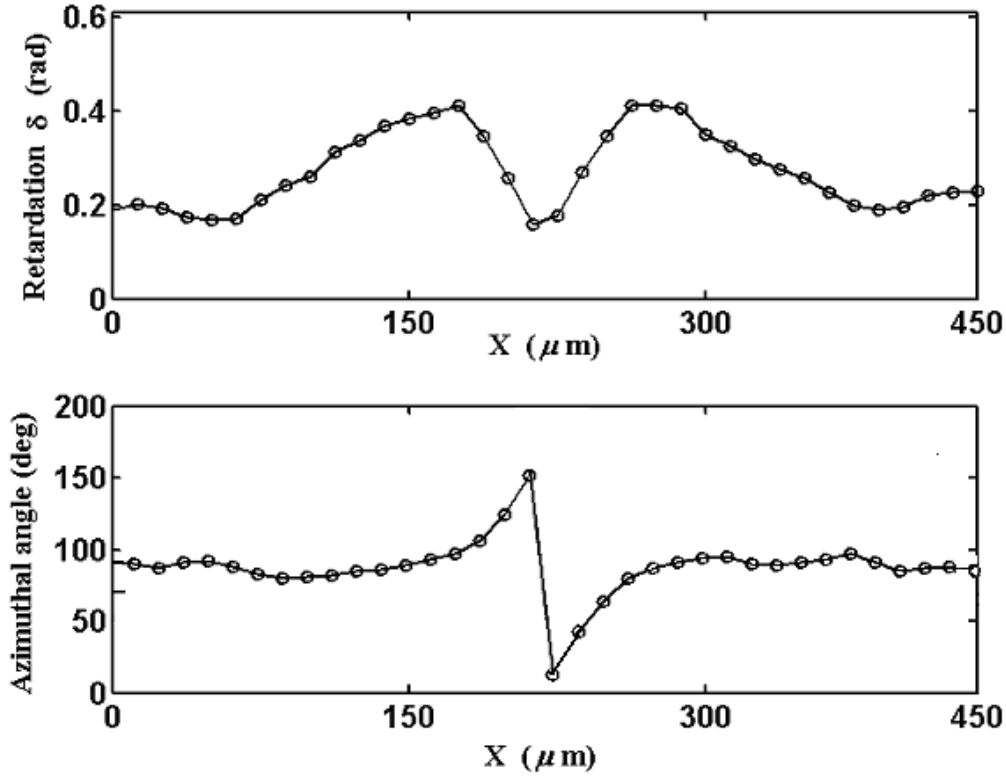

Fig . 3-4 (a) 1D profile of optical retardation along the x-axis; and (b) the profile of LC azimuthal angle across the Néel wall.

3-2 Néel wall with a point defect

Next we shall investigate the defect structure with a point defect coupling with a Néel wall. Fig.3-5 shows a protruding material on substrate, the rod-shaped LC molecules will align along this protruding structure.

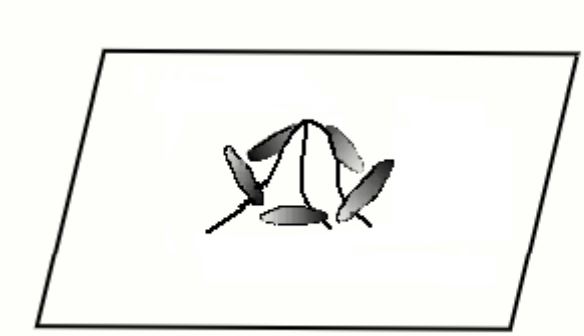

Fig .3-5 Sketch of LC molecule around a point defect.

Therefore, when a point defect couples with a Néel wall, the director arrangement of LC molecules should be similar to Fig.3-6.

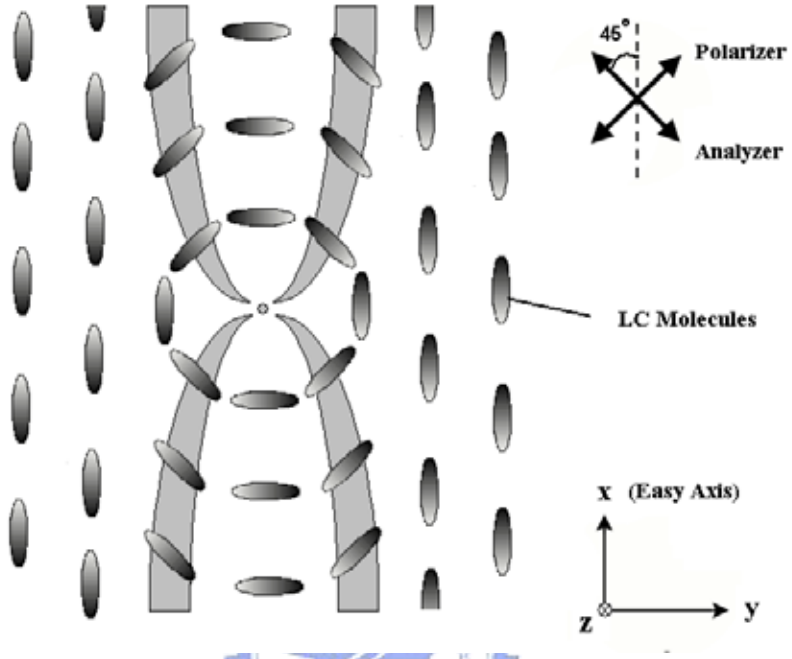

Fig.3-6 The LC configuration of a Néel wall coupled with a point defect.

We have applied our imaging polarimetric apparatus on this subject. Here is our preliminary experimental result (see Fig.3-7).

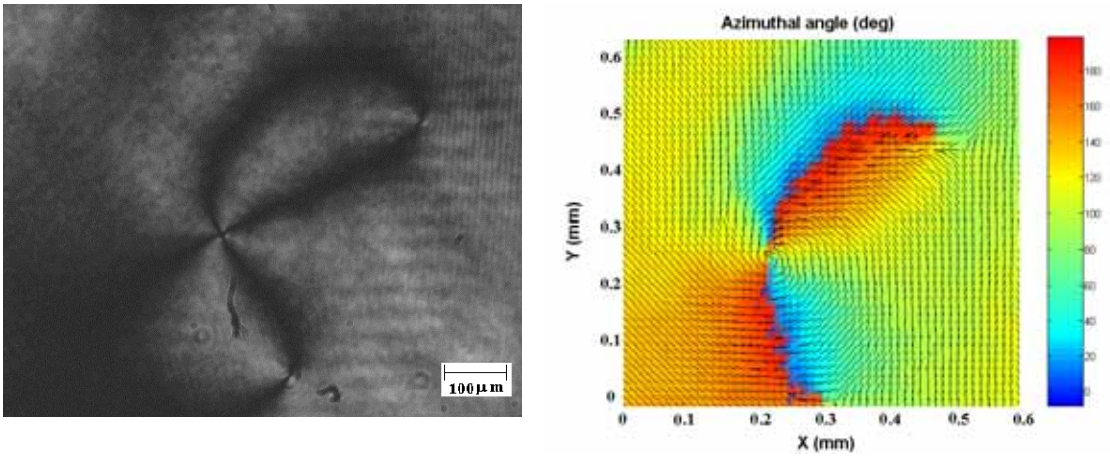

(a) (b)

Fig.3-7 (a) Image of a Néel wall coupled with a point defect under crossed polarizers; (b) the two-dimensional distribution of azimuthal angle of LC director.

3-3 Néel wall under an external electric field

Finally, we shall describe the behavior of a Néel wall under an external electric field. The direction of applied electric field is perpendicular to the substrates with alternating current (AC) voltage at 1 kHz. The LC molecules used prefer to align with the direction of electric field. The horizontally aligned LC will tilt up when applied voltage is increased.

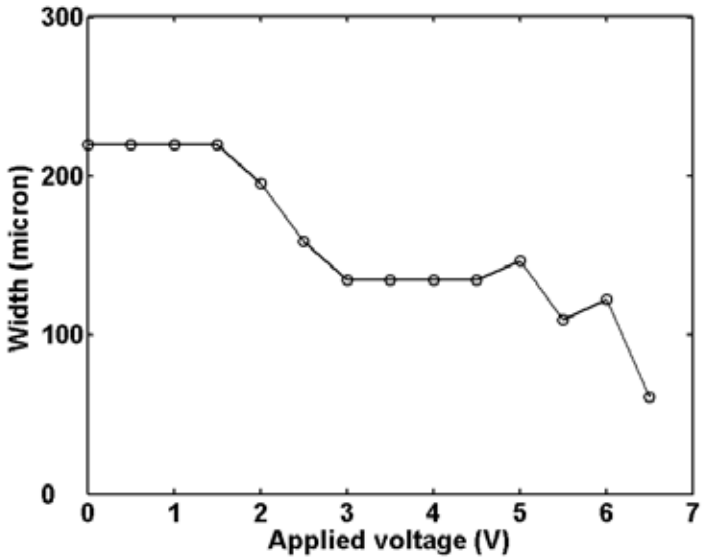

Fig.3-8 The measured width of Néel wall decreases when applied voltage is increased.

It has been observed that the width of Néel wall decreases when applied voltage is increased. The result is shown in Fig. 3-8. As pointed out above that polar angle increases with applied voltage. We can imagine that when LC molecules tilt, the applied electric field will generate a force to pull LC molecules along the easy axis, which results in a reduction in the width of Néel wall.

Chapter 4 Conclusions

In this thesis, an imaging polarimetry and data acquisition procedures are designed for determining two-dimensional distributions of the thickness and optical axis of an optical uniaxial film.

In conclusion, we demonstrate that

1) This proposed method combines an imaging polarimeter with rotation sample scheme and can be employed for monitoring film thickness from 1 μm to mm scale.
2) The proposed polarimeter had been compare with conventional conoscope.
3) This polarimeter can measure the 2D birefringence distribution, azimuthal angle, polar angle and thickness of a uniaxial crystal.
4) We successfully demonstrate the functionality with a 1-mm thick stoichiometric $LiNbO_3$ wafer, 4.9-μm thick liquid crystal device and 10-μm thick spatial light modulator (SLM).
5) This polarimeter with an in-plane spatial resolution better than 100 μm.
6) The LC director's orientation of Néel wall with and without a point defect have been observed and discussed.
7) The behavior of a Néel wall under applied electric field have been observed and discussed.

Some works remain to be done in the future:

1) Using this polarimeter to research other materials such as ferroelectric liquid crystal.

2) Using this polarimeter to research other defects such as zigzag in ferroelectric liquid crystal.

3) Detailed analysis the behavior of a Néel wall under applied voltage.

References:

[1] Yoshio Nishida and Masanobu Yamanaka, “Development of a two-dimensional birefringence distribution measurement system in laser-diode pumped solid-state laser material “, Review of Scientific Instruments **72**, 2387-2391 (2001).

[2] T. J. Scheffer and J. Nehring, “Accurate determination of liquid-crystal tilt bias angles”, J. Appl. Phys. **48**, 1783-1792 (1977).

[3] Justin S. Baba, Jung-Rae Chung, Aimee H. DeLaughter, Brent D. Cameron, Gerard L. Cote, “Development and calibration of an automated Mueller matrix polarization imaging system”, Journal of Biomedical Optics 7, 341–349 (2002).

[4] K. Jin Seog Gwag, Seo Hern Lee, Kyoung-Ho Park, Won Sang Park, Kwan-Young Han, and Chul Gyu Jhun, “Simple method for measuring the high pretilt angle of nematic liquid crystals”, J. Appl. Phys, 93, 4936-4938 (2003).

[5] Brett L. Van Horn and H. Henning Winter, “Analysis of the conoscopic measurement for uniaxial liquid-crystal tilt angles”, Appl. Opt. **40**, 2089-2094 (2001).

[6] S. T. Tang and H. S. Kwok, “Transmissive liquid crystal cell parameters measurement by spectroscopic ellipsometry”, J. Appl. Phys. **89**, 80-85 (2001).

[7] Eduardo Elizalde, J. M. Frigeio and J. Rivory, “determination of thickness and optical constants of thin films from photometric and ellipsometric measurements”, Appl. Opt. 25, 4557-4561 (1986).

[8] For example, see R. M. A. Azzam and N. M. Bashara, *Ellipsometery and Polarized Light* (North-Holland, Amsterdam, 1989).

[9] For example, see D. S. Kliger, J. W. Lewis, and C. E. Randall, *Polarized Light in Optics and Spectroscopy* (Academic Press, San Diego, CA, 1990), Chap. 4, pp. 75-83.

[10] K. Polgar, A. Peter, L. Kovacs, G. Corradi, and Z. Szaller, “Growth of stoichiometric LiNbO3 single crystals by top seeded solution growth method”, J. Cryst. Growth **177**, 211-216 (1997).

[11] K. Niwa, Y. Furukawa, S. Takekawa, and K. Kitamura, “Growth and characterization of MgO doped near stoichiometric LiNbO3 crystals as a new nonlinear optical material”, J. Cryst. Growth **208**, 493-500 (2000).

[12] SLM-128, Cambridge Research and Instrumentation Inc. (CRI), Woburn, MA, U.S.A.

[13] S. Kobayashi and Y. Iimura: Proc. SPIE **2175** (1994) 122.

[14] M. Schadt, H. Seiberle and A. Schuster: Nature **381** (1996) 212.

[15] L. M. Blinov and V. G. Chigrinov: Electrooptic Effects in Liquid Crystal Materials (Parially Ordered Systems) (Springer-Verlag, Berlin, Heidelberg, 1993)

[16] Xiang Tong Li, Dong He Pei, Shunsuke Kobayashi and Yasufumi Iimura, “ Measurement of azimuthal anchoring energy at liquid crystal/photopolymer interface”, Jpn. J. Appl. Phys. Vol. **36** (1997) pp. **L**432-**L**434.

[17] Katsuhiro Okubo, Munehiro Kimura and Tadashi Akahane, “Measurement of genuine azimuthal anchoring energy in consideration of liquid crystal molecular adsorption on alignment film”, Jpn. J. Appl. Phys. **42**,6428-6433 (2003).

[18] G. Ryschenkow and M. Kleman, “Surface defects and structural transitions in very low anchoring energy nematic thin films” The Journal of Chemical Physics, **64**No.1, 404-412 (1976).